

# Evidence for a soft-phonon-mode-driven Peierls-type distortion in $\text{Sc}_3\text{CoC}_4$

Jan Langmann,<sup>1</sup> Christof Haas,<sup>1</sup> Emmanuel Wenger,<sup>2</sup> Dominik Schaniel,<sup>2</sup> Wolfgang Scherer,<sup>1</sup> and Georg Eickerling<sup>1,\*</sup>

<sup>1</sup>*University of Augsburg, Institut für Physik, Universität Augsburg,  
Universitätsstraße 1, D-86159 Augsburg, Germany*

<sup>2</sup>*Université de Lorraine, CNRS, CRM2, F-54000 Nancy, France*

(Dated: September 9, 2020)

We provide experimental and theoretical evidence for the realization of the Peierls-type structurally distorted state in the quasi-one-dimensional superconductor  $\text{Sc}_3\text{CoC}_4$  by a phonon-softening mechanism. The transition from the high- to the final low-temperature phase below 80 K proceeds *via* an extended intermediate temperature regime between 80 K and 150 K characterized by phonon-driven atom displacements. In support of the low-dimensional character of the title compound we find a highly anisotropic correlation-length of these dynamic distortions.

## I. INTRODUCTION

Due to recent advances in nanofabrication and nanopatterning dimensionality effects in physical phenomena have become a very active field of research. Even nanowires or two-dimensional films of decidedly three-dimensional materials such as perovskites have become available for further studies.<sup>1,2</sup> Still, the majority of publications in this field is dedicated to a narrow range of materials with structurally inherent low-dimensional features. These are for example  $\text{NbSe}_3$ <sup>3-6</sup> and  $\text{K}_{0.3}\text{MoO}_3$ <sup>7-10</sup> as representatives of quasi-one-dimensional (quasi-1D) compounds and graphite/graphene<sup>11,12</sup> and transition-metal dichalcogenides<sup>13-18</sup> as representatives of quasi-two-dimensional (quasi-2D) compounds. On the one hand, this focus comes from the weak bonding between their low-dimensional building units easing the fabrication of nano-devices. On the other hand, but even more importantly, intriguing effects of the strongly anisotropic atomic interactions can already be observed in the bulk material.

A characteristic physical phenomenon in many structurally low-dimensional materials is the existence of a subtle competition between a structurally distorted state (*e.g.* due to the formation of a charge-density wave) and a superconducting state. The balance between these usually conflicting states may be influenced by external factors such as hydrostatic pressure,<sup>5,19-22</sup> rapid quenching<sup>18</sup> and chemical pressure *via* the intercalation or substitution of additional elements.<sup>17,23</sup>

The complex carbide  $\text{Sc}_3\text{CoC}_4$  represents a promising new member in this family of materials: Its structure is coined by quasi-1D infinite  $[\text{Co}(\text{C}_2)_2]$  ribbons orientated along the crystallographic *b*-axis<sup>24-31</sup> and it shows a phase transition into a superconducting state below  $T_c = 4.5$  K.<sup>27,28,30</sup> As was recently demonstrated by Wang *et al.*, the superconducting volume fraction of polycrystalline  $\text{Sc}_3\text{CoC}_4$  samples significantly increases with pressure.<sup>32</sup> At the same time, we have shown in a previous combined X-ray and neutron diffraction study that below approx. 72 K  $\text{Sc}_3\text{CoC}_4$  undergoes a Peierls-type transition to a low-temperature phase with a doubled

translational period along the  $[\text{Co}(\text{C}_2)_2]$  ribbons.<sup>27,29,30</sup> Crystallographically, the transition from the orthorhombic high-temperature (HT) phase (space group *Immm*) to the monoclinic low-temperature (LT) phase (space group *C2/m*) proceeds *via* a *t2*- followed by an *i2*-transition, leading to a systematic twinning of single crystalline samples in the LT phase.<sup>33</sup> Yet, the driving forces and the exact path to this structurally distorted LT phase remain controversial. In earlier works, we interpreted anomalies in the electrical resistivity and the magnetic susceptibility of polycrystalline  $\text{Sc}_3\text{CoC}_4$  samples as hints to the emergence of a charge-density wave (CDW) below  $\approx 140$  K.<sup>27,29,30</sup> This interpretation has been challenged by Zhang *et al.*<sup>34</sup> Their theoretical study provided no evidence of a Fermi surface instability with respect to a CDW of  $\text{Sc}_3\text{CoC}_4$  in its HT phase. In order to correlate the anomalies in the electrical transport properties with potential structural changes we performed temperature-dependent X-ray diffraction and resistivity measurements on single-crystalline  $\text{Sc}_3\text{CoC}_4$  samples.

## II. METHODS

Single crystals of  $\text{Sc}_3\text{CoC}_4$  were grown according to methods described in the literature<sup>26,31,33</sup> and in addition from a lithium metal flux.<sup>35</sup> Needle-like samples with a thickness of  $\approx 20$   $\mu\text{m}$  and a length of  $\approx 200$   $\mu\text{m}$  were obtained from the first method and platelet-like samples with a thickness of  $\approx 150$   $\mu\text{m}$  and a lateral size of  $\approx 300$   $\mu\text{m}$  from the latter. X-ray diffraction measurements<sup>36</sup> of the temperature dependent superstructure reflection intensities ( $10 \text{ K} < T < 160 \text{ K}$ ) were performed on a HUBER eulerian cradle equipped with a MAR345 image-plate detector and operated at the window of a BRUKER FR591 rotating anode (Mo  $\text{K}_\alpha$ ). Additional temperature-dependent single crystal data ( $T > 100 \text{ K}$ ) was collected on a BRUKER-NONIUS  $\kappa$ -goniometer operated at the window of an INCOATEC MicroFocus Tube (Mo  $\text{K}_\alpha$ ). Mapping of diffuse scattering intensities was done employing a HUBER eulerian cradle goniometer equipped with an INCOATEC MicroFocus Tube (Ag  $\text{K}_\alpha$ ) and a PILATUS 300K CdTe de-

tector. Cryogenic temperatures  $T > 80$  K were generated by a standard OXFORD open-flow  $N_2$  cooler,<sup>37</sup> measurements at  $T < 80$  K were performed employing an ARS closed-cycle He-cryostat. The handling of parasitic scattering from the vacuum and radiation shields in the closed-cycle cryostat (beryllium domes) was described elsewhere.<sup>38</sup> Numerical values for the intensities of representative superstructure reflections and diffuse features were extracted by image analysis of the collected X-ray diffraction data.

Resistivity measurements of single crystals of  $Sc_3CoC_4$  contacted in a four-point geometry were carried out using a Physical Property Measurement System (PPMS, QUANTUM DESIGN).

Geometry relaxations of the HT and LT phase of  $Sc_3CoC_4$  starting from the structural parameters from Eickerling *et al.*<sup>30</sup> were performed employing the VASP code.<sup>39–42</sup> The PBE density functional was used throughout,<sup>43,44</sup> the energy cutoff for the plane wave basis set was set to 550 eV and a Brillouin grid sampling of  $4 \times 4 \times 2$  and  $2 \times 2 \times 2$  was used for the HT- and LT-phase, respectively. Optimizations were stopped when forces were smaller than 0.001 eV/Å.

The PHONOPY code<sup>45</sup> was used for phonon dispersion calculations on  $Sc_3CoC_4$  with a  $2 \times 2 \times 2$  supercell. Forces were calculated with the VASP program employing the PBE density functional<sup>43,44</sup>, a  $4 \times 4 \times 2$   $k$ -point mesh and an energy cutoff for the plane wave basis set of 500 eV.<sup>39–42</sup> Temperature-dependent thermal diffuse scattering (TDS) simulations were obtained using the *ab2tds* code.<sup>46</sup> The phonon eigenvectors underlying the simulations were generated with PHONOPY on a  $24 \times 24 \times 22$   $q$ -mesh (containing  $\Gamma$ ). In *ab2tds*, the Fourier transform of the dynamical matrix was calculated on a  $9 \times 9 \times 9$  mesh of points. Debye-Waller factors for each temperature were computed and reciprocal space planes of TDS intensity were sampled on  $100 \times 100$   $q$ -points for a wavelength of 0.56087 Å and a lower eigenvalue-cutoff of 0.001 meV.

### III. ELECTRICAL RESISTIVITY

We focus on the results of the electrical resistivity measurements on single crystalline samples of  $Sc_3CoC_4$  first (see Fig. 1a). In accordance with earlier resistivity data from polycrystalline samples,<sup>27,30</sup> two anomalies are observed at  $T \approx 82$  K and 149 K. At both temperatures, the overall metallic decrease of  $\rho(T)$  is interrupted by a local increase of the resistivity. The anomaly at 82 K is discerned by a sharp jump in  $\rho(T)$  and corresponds to an irreversibility in  $\rho(T)$  for polycrystalline samples that permanently displaces the heating against the cooling curve.<sup>27,30</sup> This contrasts with the broader and more gradual character of the anomaly at 149 K.

Details about structural changes connected to the two anomalies in the electrical resistivity are provided by the results of detailed temperature-dependent single-crystal

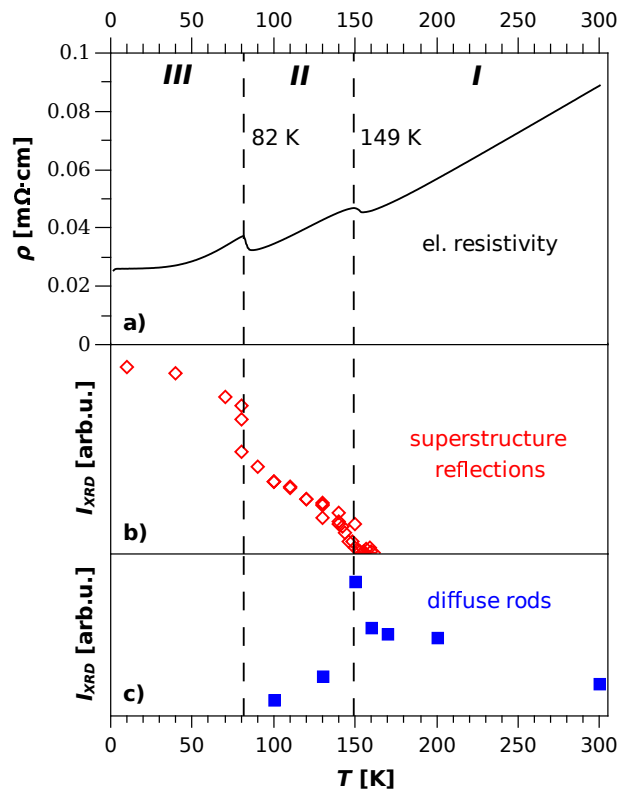


FIG. 1. Temperature-dependence of (a) the electrical resistivity  $\rho(T)$ , (b) the X-ray scattering intensity of superstructure reflections and (c) the X-ray scattering intensity of diffuse rods  $I_{XRD}(T)$  connecting the superstructure reflection positions along  $c^*$ .

X-ray diffraction measurements on  $Sc_3CoC_4$  outlined in the following.

### IV. X-RAY DIFFRACTION

A concise analysis of temperature-dependent changes in diffraction space allows insight into the evolution of the LT structure of  $Sc_3CoC_4$  from the HT structure. The intensity of the superstructure reflections  $I_{XRD}(T)$  with  $k = (\pm\frac{1}{2}, \pm\frac{1}{2}, 0)$  that result from a fourfold enlargement of the orthorhombic HT unit cell in its  $ab$ -plane<sup>33</sup> represents an appropriate order parameter for the transition from the HT to the LT structure. The simultaneous existence of additional reflections at  $k = (+\frac{1}{2}, +\frac{1}{2}, 0)$  and  $k = (+\frac{1}{2}, -\frac{1}{2}, 0)$  is due to the systematic twinning caused by the  $t2$ -transition. Note, that all real space and reciprocal space coordinates given hereafter are referred to the orthorhombic HT-phase unit cell.

Our measurements reveal an increase of  $I_{XRD}(T)$  (see Fig. 1b) in two phenomenologically distinct steps at temperatures between 150 K and 80 K.<sup>47</sup> Thereby,  $T \approx 150$  K marks the onset of  $I_{XRD}(T)$  followed by a steady increase down to 80 K. At about 80 K, a sharp jump of  $I_{XRD}(T)$  is observed. Further cooling towards 10 K

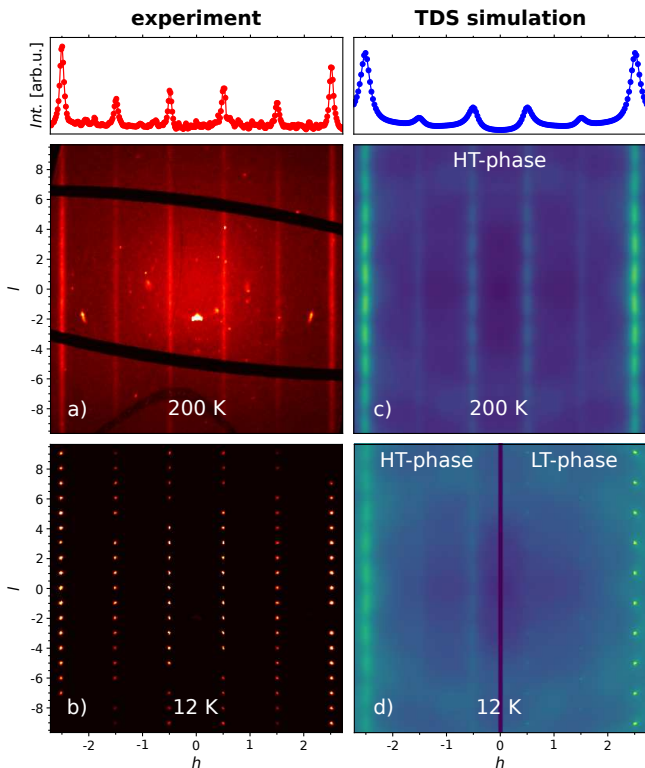


FIG. 2. Comparison of the X-ray scattering features in the  $(h, 1.5, l)$ -plane of  $\text{Sc}_3\text{CoC}_4$  as obtained from experiments at different temperatures (a and b) and thermal diffuse scattering (TDS) simulations based on *ab-initio* calculated phonon dispersion relations for the HT-phase structure (c and left part of d) and the LT-phase structure of  $\text{Sc}_3\text{CoC}_4$  (right part of d). Note that the Miller indices refer to the orthorhombic HT-phase and that twinning was not considered in the calculations. 1D-profiles of (a) and (c) at  $l \approx 2$  are given in the top panel. For details on the simulations, see main text.

entails a saturation of  $I_{XRD}(T)$  already below  $\approx 70$  K. We note the close resemblance of this temperature-dependence of the superstructure reflection intensity to the observed behavior of  $I_{XRD}(T)$  in the charge-density wave material  $2H\text{-TaSe}_2$ .<sup>48–50</sup> In this compound, a sharp step in the superstructure reflection intensities marks a lock-in transition from an incommensurate modulation of the atomic positions at higher temperatures to a commensurate modulation at lower temperatures<sup>48–50</sup>. However, within the available experimental accuracy we could not find hints to the existence of an incommensurate phase in  $\text{Sc}_3\text{CoC}_4$ , *i.e.* significant temperature-dependent changes in the superstructure reflection positions or the appearance of higher-order satellite reflections. This puts  $\text{Sc}_3\text{CoC}_4$  in a row with the extensively studied transition-metal dichalcogenide  $1T\text{-TiSe}_2$  that shows a Peierls-type structural distortion with a twofold commensurate modulation wave vector  $k$  down to a temperature of 8.3 K.<sup>15,51–59</sup>

Adding to the pinpoint superstructure reflections strongly temperature-dependent diffuse rods connecting

the superstructure reflection positions along  $c^*$  can be observed for  $\text{Sc}_3\text{CoC}_4$ . Representative  $(h, 1.5, l)$  reciprocal space planes reconstructed from measuring data at 200 K and 12 K and showing exclusively superstructure reflections and diffuse rods are shown in Fig. 2a-b.<sup>36</sup> Above 200 K, diffuse rod-shaped features without significant intensity modulation along  $c^*$  are observed. Upon cooling towards 80 K, a monotonous increase of the intensity at the superstructure reflection positions is paralleled by a lambda-shaped peaking of the diffuse intensity between the superstructure reflection positions at 150 K and its subsequent decay to zero (see Fig. 1c).<sup>47</sup> Below 80 K, only intensity at the superstructure reflection positions remains. This marked temperature-dependence along with an anomalous modulation of the diffuse intensity with varying  $h$ -index (indicated by the profile in the top-panel of Fig. 2a) rules out crystal defects (*e.g.* stacking disorder) as the predominant origin of these diffuse features. A detailed discussion of the characteristic variation of the diffuse intensity in reciprocal space can be found in Appendix B.

Moreover, the coinciding positions of both, diffuse rods and pinpoint superstructure reflections, can be taken as a hint to their common origin. Similar transitions from precursor diffuse features in reciprocal space to pinpoint superstructure reflections are known for other structurally low-dimensional materials featuring low-temperature periodic distortions, *e.g.*  $1T\text{-TaS}_2$ ,<sup>13,60</sup>  $\text{K}_{0.3}\text{MoO}_3$ <sup>9,61</sup> or  $\text{NbSe}_3$ .<sup>61,62</sup>

Based on the temperature-dependent changes in diffraction space, three different temperature regimes for the structural properties of  $\text{Sc}_3\text{CoC}_4$  may be assigned: **(I)** a HT-regime above  $\approx 150$  K characterized by unmodulated (or only weakly) modulated diffuse rods along  $c^*$  in reciprocal space, **(II)** a pre-LT-regime between  $\approx 150$  K and  $\approx 80$  K with coexistent diffuse rods and weak superstructure reflections, and **(III)** a LT-regime below  $\approx 80$  K marked by the exclusive presence of strong and pinpoint superstructure reflections. This partitioning into temperature regimes fits equally well with the anomalies in the electrical resistivity  $\rho(T)$  (see Fig. 1a). More specifically, the steady transition between **(I)** and **(II)** in  $I_{XRD}(T)$  is reflected by a broad uprise in  $\rho(T)$  at 149 K. At the same time, the step-like increase of  $I_{XRD}(T)$  between **(II)** and **(III)** relates to the sharp increase in  $\rho(T)$  at 82 K. The differing nature of the transitions at around 80 K and 150 K is further emphasized by powder neutron diffraction studies on  $\text{Sc}_3\text{CoC}_4$  performed earlier.<sup>30</sup> Therein, step-like lattice parameter changes with sudden increases in  $b$  and  $c$  and a decrease in  $a$  were observed upon cooling of the samples to below 80 K. There was no evidence for a comparable anomaly in  $a$ ,  $b$  and  $c$  in the temperature region around 150 K.

## V. DISCUSSION

Starting point for the interpretation of the above results is the structural model of the  $\text{Sc}_3\text{CoC}_4$  HT-phase. The existence of rod-shaped features in diffraction space may be related to layered structural moieties in real space. Taking into account the orientation of the rods along  $c^*$ , these layers must extend parallel to the crystallographic  $ab$ -plane of the orthorhombic HT cell and can be associated with stacked ribbons of interconnected  $[\text{Co}(\text{C}_2)_2\text{Co}]$  hexagons (shaded in red and green in Fig. 3a).

In a simplistic picture, the diffuse rods may be attributed to disorder between the layered building units of the HT-structure along  $c$ . However, the characteristic intensity modulation of the rod intensity perpendicular to  $c^*$  (see profile above Fig. 2a) precludes an explanation in terms of a static stacking disorder involving the slippage of complete layers (see Appendix B). An alternative explanation for the occurrence of diffuse intensity above 80 K might be provided by precursor dynamic fluctuations along the displacement coordinates of the static Peierls-type distortion evolving below 80 K. The temperature-dependent contraction of the diffuse intensity into superstructure reflections between 150 K and 80 K may in turn be linked to the softening of a phonon mode at  $k = (\frac{1}{2}, \frac{1}{2}, 0)$ .<sup>30</sup>

In Fig. 4 the phonon dispersion of  $\text{Sc}_3\text{CoC}_4$  is shown along selected lines of the first Brillouin-Zone (BZ) of the orthorhombic HT phase. Along the path W  $(\frac{1}{2}, \frac{1}{2}, 0)$ –T  $(\frac{1}{2}, \frac{1}{2}, \frac{1}{2})$  a low-frequency branch with marginal dispersion can be identified. The displacement pattern corresponding to the mode at W is in close analogy to the static displacement pattern in the LT-phase of  $\text{Sc}_3\text{CoC}_4$ .<sup>30</sup> Furthermore, the path W–T of the low-lying phonon branch can be correlated with the course of the diffuse rods in reciprocal space (see Appendix A).<sup>63,64</sup> Figuratively, its flat course can be interpreted in terms of equal excitation energies for an infinite set of dynamic LT-phase-like displacements of the cobalt and scandium atoms (illustrated in Fig. 3b for a layer section in the  $ab$ -plane) with differing modulations along the stacking direction  $c$ .<sup>65</sup> The superposition of all these dynamic displacements yields the picture of disorder between the layered building units of  $\text{Sc}_3\text{CoC}_4$ . In fact, similar behavior connected to weak coupling between layered building units has been observed for other compounds such as the francisite  $\text{Cu}_3\text{Bi}(\text{SeO}_3)_2\text{O}_2\text{Cl}$ . In the phonon dispersion of its HT-phase, a nearly dispersionless branch connects a zone-center mode at  $\Gamma$  with equal atom displacements in all constituting layers to a modulated variant of the mode at Z with layer-wise inverted atom displacements.<sup>66</sup>

To underline the correspondence between diffuse rods in X-ray diffraction and a soft branch in the phonon dispersion we performed simulations of the thermal diffuse scattering (TDS) contribution to the diffracted intensity in the  $(h, 1.5, l)$ -plane. Consistent with the inferences made above, simulations based on the phonon dispersion

of the HT-phase of  $\text{Sc}_3\text{CoC}_4$  and assuming a temperature of 200 K (Fig. 4) reproduce the experimental observations not only in the general positions and direction of the rods, but even in details like the non-trivial intensity variations along the  $a^*$  direction. A comparison between the experimentally obtained  $(h, 1.5, l)$ -plane at 200 K and the TDS simulation for the HT-phase of  $\text{Sc}_3\text{CoC}_4$  is given in Figs. 2a and c with corresponding profiles in the top panel. The weak modulation of the simulated TDS intensity with a period of two reciprocal lattice constants along  $c^*$  in Fig. 2c is most likely due to numerical artifacts introduced by a Fourier interpolation step and not supported by reciprocal space reconstructions based on X-ray diffraction data.<sup>67</sup>

The phonon dispersion of the HT-phase of  $\text{Sc}_3\text{CoC}_4$ , however, cannot explain the gradual vanishing of the diffuse rods between 150 K and 80 K and the appearance of pinpoint superstructure reflections. Fig. 2b shows a reconstruction of the  $(h, 1.5, l)$ -plane from measuring data at 12 K illustrating the extensive reorganization of the X-ray diffraction pattern below 80 K. To account for these changes, a phonon softening mechanism may be invoked that selectively reduces the frequency of the phonon mode at W in the soft W–T branch to zero. Simultaneously with the increasing dispersion between W and T comes a preference for LT-phase-like dynamic atom displacements without superimposed modulation along  $c$  and a progressive structural ordering. Zero phonon frequency at W is reached at 80 K resulting in the formation of the LT-phase of  $\text{Sc}_3\text{CoC}_4$  with static atom displacements from the equilibrium positions in the HT-phase. Consequently, no more prominent diffuse features are found in TDS simulations of the  $(h, 1.5, l)$ -plane at 12 K employing the phonon eigenvalues of the LT-phase<sup>30</sup> (see right part of Fig. 2d).<sup>68</sup> Only localized TDS contributions at positions of the experimentally observed superstructure reflections remain, consistent with a doubling of the unit cell. We note, that twinning was not considered within the simulations and thus each second reflection position is missing in Fig. 2d. That the rearrangement of diffuse features in reciprocal space cannot be attributed to temperature effects alone is illustrated by TDS simulations for the HT-phase structure of  $\text{Sc}_3\text{CoC}_4$  at 12 K (left part of Fig. 2d). Without a structural transition weak diffuse rods would still be present at this temperature. Again, parallels to the francisite  $\text{Cu}_3\text{Bi}(\text{SeO}_3)_2\text{O}_2\text{Cl}$  may be drawn, where cooling induces a successive frequency reduction of the phonon mode at Z in the soft  $\Gamma$ -Z branch setting the stage to a displacive transition into a static LT-phase with doubled  $c$ -parameter at 115 K.<sup>66,69</sup>

We may thus propose a consistent model for the observations in electrical resistivity and intensity-weighted reciprocal space: In the HT-regime (**I**, see Fig. 1) above 150 K, dynamic disorder driven by the phonon modes W–T leads to the occurrence of diffuse rods in reciprocal space. At approx. 150 K, the mode at W starts to soften, thus continuously reducing the degree of thermal fluctuations in the pre-LT regime (**II**) and leading to the

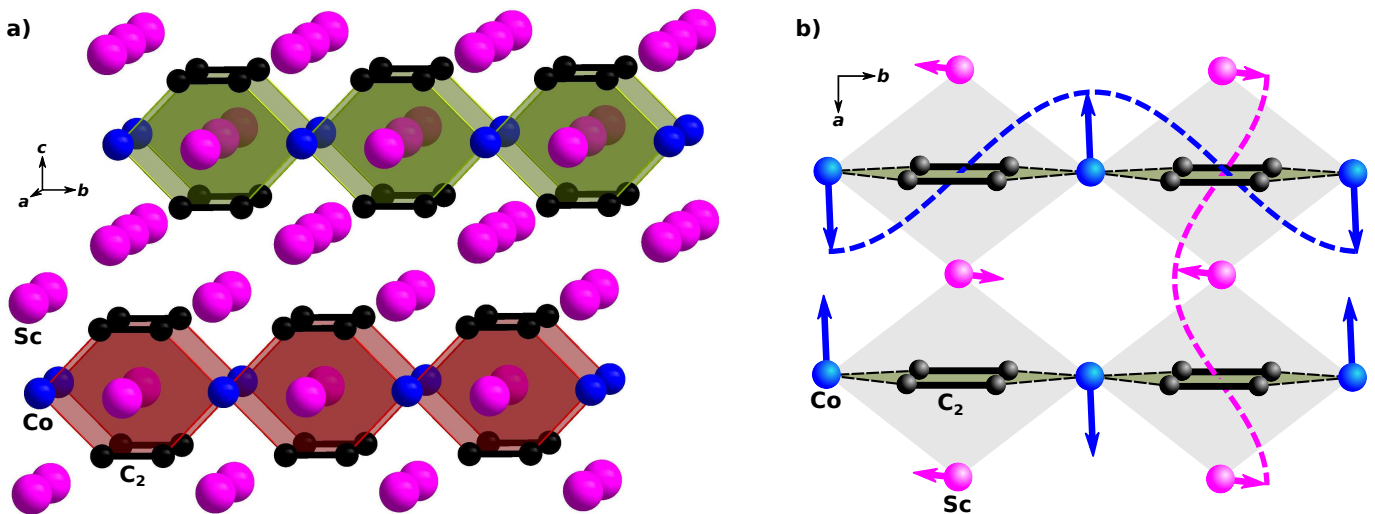


FIG. 3. Ball-and-stick representation of the layered building units of HT  $\text{Sc}_3\text{CoC}_4$  in (a) the crystallographic  $bc$ -plane and (b) the crystallographic  $ab$ -plane of the orthorhombic unit cell. In (b) the sinusoidal displacive modulation of the cobalt and scandium atom positions as observed for the low-frequency phonon modes between W and T (see text) and the monoclinic LT-phase<sup>30</sup> is indicated by arrows.

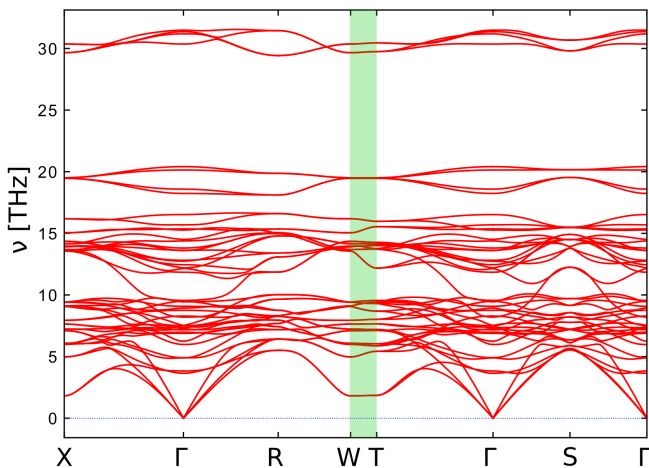


FIG. 4. Calculated phonon dispersion along selected high-symmetry paths in the Brillouin zone of HT  $\text{Sc}_3\text{CoC}_4$ . The path between W  $(\frac{1}{2}, \frac{1}{2}, 0)$  and T  $(\frac{1}{2}, \frac{1}{2}, \frac{1}{2})$  is highlighted.

successive ordering of the layers stacked in  $c$  direction. Around 80 K, the softening process is complete and the displacement pattern of the phonon mode freezes into the static atomic positions observed in the LT-phase (**III**) of  $\text{Sc}_3\text{CoC}_4$ .

## VI. CONCLUSION

To conclude, we provide experimental and theoretical evidence for a soft-phonon-driven formation of a Peierls-type structurally distorted state in  $\text{Sc}_3\text{CoC}_4$  upon cooling. Based on the new results, the interplay between two distinct transitions, *i.e.* a charge-density wave transition

at 150 K and a Peierls-type distortion at 80 K, discussed in earlier publications<sup>27,29,30,34</sup> can now be consistently described by a single extended structural phase transition *via* an intermediate state between 80 K and 150 K. This intermediate state is characterized by phonon-driven dynamic atom displacements in the crystallographic  $ab$ -plane with strongly temperature-dependent frequency and correlation-length along the  $c$ -axis. Inelastic X-ray or neutron scattering experiments might provide further information on the progression of the phonon-softening mechanism towards the static structurally distorted LT-phase observed below 80 K.

### Appendix A: Interpretation of diffuse X-ray scattering intensity – Relation to the phonon dispersion

In the following, we outline the theoretical background for the interpretation of the diffuse rods observed in reciprocal space for  $\text{Sc}_3\text{CoC}_4$  in temperature regimes **I** and **II** (above  $\approx 80$  K) in terms of Thermal Diffuse Scattering (TDS).

We focus on the first-order TDS intensity given by the sum over the absolute squares of the dynamical structure factor contributions  $F_j$  for all phonons  $j$

$$I_1(\mathbf{q}) = \frac{\hbar N I_e}{2} \sum_j \frac{1}{\omega_{\mathbf{q},j}} \coth\left(\frac{\hbar\omega_{\mathbf{q},j}}{2k_B T}\right) |F_j(\mathbf{q})|^2 \quad (\text{A1})$$

where the number of unit cells is denoted by  $N$  and the one-electron scattering intensity by  $I_e$ . Every sum contribution is weighted by a thermal occupation factor

$\frac{1}{\omega_{\mathbf{q},j}} \coth\left(\frac{\hbar\omega_{\mathbf{q},j}}{2k_B T}\right)$  for phonon  $j$  at wave vector  $\mathbf{q}$  with frequency  $\omega_{\mathbf{q},j}$ .<sup>64</sup> Thus, the contributions of low-frequency phonons to TDS are dominant. The dynamical structure factors  $F_j$  derive from the phonon-specific shift of the atoms  $s$  in the unit cell as

$$F_j(\mathbf{q}) = \sum_s \frac{f_s}{\sqrt{\mu_s}} \exp(-M_s) (\mathbf{q} \cdot \mathbf{e}_{\mathbf{q},j,s}) \quad (\text{A2})$$

with atomic scattering factor  $f_s$ , atomic mass  $\mu_s$  and Debye-Waller factor  $M_s$ . Size and direction of the atom shifts are described by the polarization vector  $\mathbf{e}_{\mathbf{q},j,s}$ .<sup>64</sup> Special attention should be paid to the double meaning of the wave vector  $\mathbf{q}$ : On the one hand,  $\mathbf{q}$  is the sum of the reduced phonon wave vector in the first Brillouin zone  $\mathbf{k}$  and a reciprocal lattice vector  $\mathbf{K}_{\mathbf{q}}$

$$\mathbf{q} = \mathbf{k} + \mathbf{K}_{\mathbf{q}} \quad (\text{A3})$$

Due to the periodicity of the phonon dispersion in reciprocal space,  $\omega_{\mathbf{q},j}$  and  $\omega_{\mathbf{k},j}$  are identical. On the other hand,  $\mathbf{q}$  indicates the position of the considered TDS feature and  $\mathbf{K}_{\mathbf{q}}$  the position of the adjacent Bragg reflection in reciprocal space.

The dominant diffuse reciprocal space features in the HT regime of  $\text{Sc}_3\text{CoC}_4$  are the rods along  $c^*$ . The location of all points on the diffuse rods with respect to the adjacent Bragg reflections can be described by wave vectors  $\mathbf{k} = (\frac{1}{2}, \frac{1}{2}, l)$  with  $l$  varying between 0 and  $\frac{1}{2}$ . Thereby, the boundary points  $\mathbf{k} = (\frac{1}{2}, \frac{1}{2}, 0)$  and  $\mathbf{k} = (\frac{1}{2}, \frac{1}{2}, \frac{1}{2})$  represent positions on and exactly midway between the superstructure reflections appearing in the pre-LT and LT regime. From this information, a low-frequency, flat phonon branch connecting the zone-boundaries at W ( $\hat{=} (\frac{1}{2}, \frac{1}{2}, 0)$ ) and T ( $\hat{=} (\frac{1}{2}, \frac{1}{2}, \frac{1}{2})$ ) may be postulated for the HT regime. Indeed, an acoustic phonon mode with extraordinarily low frequency between W and T is found in the ab-initio phonon dispersion relation based on the idealized ground-state structure of HT  $\text{Sc}_3\text{CoC}_4$  (highlighted in green in Fig. 4).

### Appendix B: Interpretation of diffuse X-ray scattering intensity – Intensity modulations

Focusing on the intensity modulation of the TDS, diffuse rods and pinpoint superstructure reflections show similar intensity alternations along the reciprocal space directions  $a^*$  and  $b^*$  (see Fig. 2). More specifically, rows of weaker superstructure reflections or diffuse rods along  $c^*$  are invariably followed by rows of stronger superstructure reflections or diffuse rods and vice versa. Thereby, the intensity of both, weak and strong reciprocal space features, rises with increasing  $h$ - or  $k$ -index. In Fig. 5, representative line profiles of the scattering intensity along  $[h, 1.5, 0]$  cutting through the superstructure

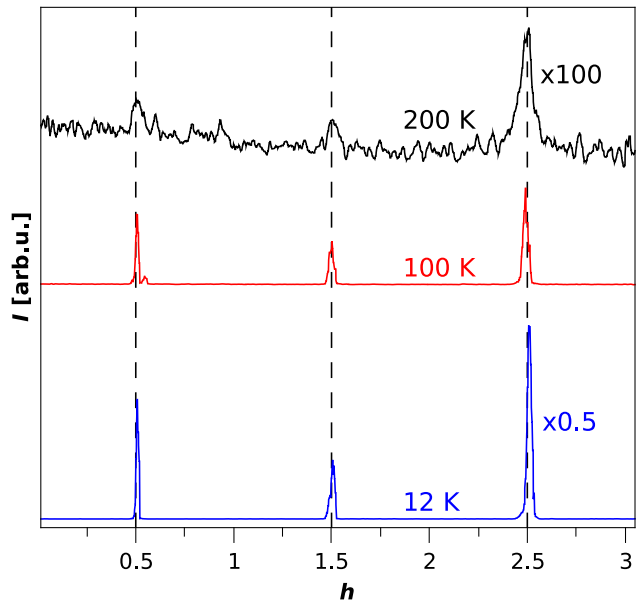


FIG. 5. Intensity profiles along  $[h, 1.5, 0]$  at 200 K (HT regime), at 100 K (pre-LT regime) and at 12 K (LT regime). All reflection indices refer to the orthorhombic HT-phase unit cell of  $\text{Sc}_3\text{CoC}_4$ . For clarity, the profiles at 200 K and 12 K were scaled by factors of 100 and 0.5, respectively. In all cases, an alternation between strong and weak intensity along  $h$  becomes evident.

reflection positions in the  $(h, 1.5, l)$ -plane are shown for each of the temperature regimes of  $\text{Sc}_3\text{CoC}_4$  postulated in section V. The similarity of the line profiles in Fig. 5 may be taken as a hint to (i) the common origin of diffuse rods and pinpoint superstructure reflections and (ii) a persistent displacive modulation of the atom positions in the  $ab$ -plane with temperature-dependent correlation length along  $c$  as opposed to simple stacking disorder.

In the following, we will relate the characteristic scattering intensity variation along the line  $[h, 1.5, 0]$  to a simplified model of the displacive modulation pattern in  $\text{Sc}_3\text{CoC}_4$ . Only scattering contributions from the set of atoms most affected by shifts from their high-symmetry positions, *i.e.* the cobalt and the scandium atoms capping the  $[\text{Co}(\text{C}_2)_2\text{Co}]$  hexagons (see Fig. 3), are taken into account. The effect of the shifts in the carbon atom positions is neglected due to the relatively small scattering cross-section of carbon compared to scandium and cobalt. Furthermore, only the scattering contributions from one of two twin domains are considered (*vide supra*). The contributions of the second domain may be symmetry-generated by application of the according twin law.

In a first step, the contributions of the cobalt and scandium atoms to the structure factor  $F(\mathbf{h})$  are treated separately. The general structure factor equation for a one-atom structure subjected to an arbitrary displacement wave is detailed elsewhere.<sup>70,71</sup> Assuming a perfectly commensurate modulation the structure factor of

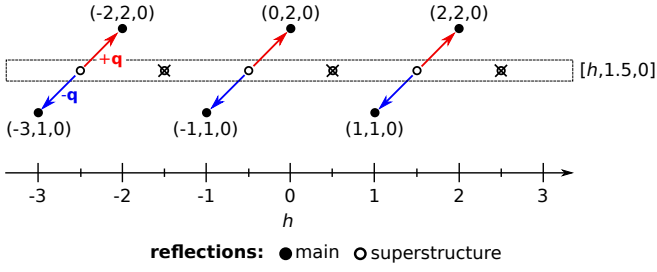


FIG. 6. Position of the main reflections in the  $(h, k, 0)$ -plane contributing to the structure factor of the superstructure reflections along the line  $[h, 1.5, 0]$ . All reflection indices are referred to the orthorhombic HT-phase unit cell of  $\text{Sc}_3\text{CoC}_4$ . The wave vectors  $+\mathbf{q}$  and  $-\mathbf{q}$  connecting the superstructure reflections to the main reflections are displayed in red and blue, respectively. Absent superstructure reflections are crossed out (see text).

$\text{Sc}_3\text{CoC}_4$  at the position of superstructure reflections can be described by the simplified formula

$$F(\mathbf{h}) = J_1(2\pi\mathbf{h}\mathbf{a}) \exp(i\phi) G(\mathbf{h} + \mathbf{q}) - J_1(2\pi\mathbf{h}\mathbf{a}) \exp(-i\phi) G(\mathbf{h} - \mathbf{q}) \quad (\text{B1})$$

The position of the superstructure reflections is referred to by the reciprocal space vector  $\mathbf{h}$ , while  $J_1(2\pi\mathbf{h}\mathbf{a})$  and  $G(\mathbf{h})$  denote the structure factor of the unmodulated structure and the first-order Bessel function, respectively. The displacement wave is characterized by its amplitude vector  $\mathbf{a}$ , wave vector  $\mathbf{q}$  and phase  $\phi$ .

Concerning the cobalt substructure, a phase  $\phi = 0$  may be put for the displacements<sup>72</sup> leading to

$$F_{\text{Co}}(\mathbf{h}) = J_1(2\pi\mathbf{h}\mathbf{a}) \cdot G_{\text{Co}}(\mathbf{h} + \mathbf{q}) - J_1(2\pi\mathbf{h}\mathbf{a}) \cdot G_{\text{Co}}(\mathbf{h} - \mathbf{q}) \quad (\text{B2})$$

so that in a first step the variation of  $J_1(2\pi\mathbf{h}\mathbf{a})$  and  $G(\mathbf{h})$  along the line  $[h, 1.5, 0]$  must be considered. As the cobalt atom displacements are directed along the crystallographic  $a$ -direction ( $\mathbf{a} = (a, 0, 0)^T$ ), the argument of  $J_1$  reduces to the scalar  $ha$ . Non-zero values of  $G_{\text{Co}}(\mathbf{h} \pm \mathbf{q})$  may only occur, if a vector  $\pm\mathbf{q} = \pm(0.5, 0.5, 0)^T$  connects the reciprocal space position  $\mathbf{h}$  of the considered superstructure reflection to the position of a non-extinct main reflection.<sup>73</sup> In accord with the two possible signs of  $\mathbf{q}$ , there are always two contributing main reflection positions in the  $(h, k, 0)$ -plane for each superstructure reflection (see Fig. 6).

However, every second superstructure reflection along  $[h, 1.5, 0]$  is absent (crossed out in Fig. 6), because its associated main reflections are extinct due to the body-centering of the HT  $\text{Sc}_3\text{CoC}_4$  crystal structure. Due to the small variation of the atomic scattering factors over the narrow considered range of  $h$ -values the structure factors  $G_{\text{Co}}(\mathbf{h} \pm \mathbf{q})$  for the contributing main reflections of the unmodulated Co substructure<sup>74</sup> depend only weakly on  $h$  with  $G_{\text{Co}}(\mathbf{h} + \mathbf{q}) > 0$  and  $G_{\text{Co}}(\mathbf{h} - \mathbf{q}) \approx -G_{\text{Co}}(\mathbf{h} + \mathbf{q})$ . Thus, the variation of the superstructure reflection structure factor  $F_{\text{Co}}(\mathbf{h})$  along  $[h, 1.5, 0]$  in good approximation mirrors the behavior of the Bessel function  $J_1(2\pi ha)$  (see solid blue line in Fig. 7a).

The same strategy can be applied in the derivation of the structure factor contribution of the scandium atoms  $F_{\text{Sc}}(\mathbf{h})$ . Displacements of the scandium atoms towards long Co  $\cdot$  Co contacts<sup>75</sup> are accounted for by putting a value of  $\pi$  for the displacement wave phase  $\phi$ , so that

$$F_{\text{Sc}}(\mathbf{h}) = -J_1(2\pi\mathbf{h}\mathbf{a}) \cdot G_{\text{Sc}}(\mathbf{h} + \mathbf{q}) + J_1(2\pi\mathbf{h}\mathbf{a}) \cdot G_{\text{Sc}}(\mathbf{h} - \mathbf{q}) \quad (\text{B3})$$

is obtained. In contrast to the cobalt atoms, the scandium atom displacements point along the crystallographic  $b$ -direction ( $\mathbf{a} = (0, a, 0)^T$ ), so that the argument  $\mathbf{h}\mathbf{a}$  of the Bessel functions in Eq. B3 is constant along  $[h, 1.5, 0]$  and  $J_1(\mathbf{h}\mathbf{a}) = \text{const.} > 0$  over the whole range of  $h$ -values. Approximating the structure factor for the contributing main reflections of the unmodulated scandium substructure<sup>76</sup> in analogy to the cobalt atom substructure again yields a weakly  $h$ -dependent value of  $G_{\text{Sc}}(\mathbf{h} \pm \mathbf{q})$  with  $G_{\text{Sc}}(\mathbf{h} + \mathbf{q}) > 0$  and  $G_{\text{Sc}}(\mathbf{h} - \mathbf{q}) \approx -G_{\text{Sc}}(\mathbf{h} + \mathbf{q})$ . Therefore, the structure factor contribution  $F_{\text{Sc}}(\mathbf{h})$  of the Sc atoms at the superstructure reflection positions along  $[h, 1.5, 0]$  shows only slight variation with  $h$  and is invariably negative (see solid red line in Fig. 7a). Finally, the structure factor contributions  $F_{\text{Co}}(\mathbf{h})$  and  $F_{\text{Sc}}(\mathbf{h})$  of cobalt and scandium along  $[h, 1.5, 0]$  can be summed up and also the structure factor contributions of the second  $\text{Sc}_3\text{CoC}_4$  domain can be generated at this stage by mirroring the contributions from the first domain at the  $y$ -axis<sup>77</sup> (hatched lines in Fig. 7a). At every second superstructure reflection position (counted from  $h = 0$ ) opposite signs of  $F_{\text{Sc}}(\mathbf{h})$  and  $F_{\text{Co}}(\mathbf{h})$  meet to yield a small absolute value of the total structure factor  $F(\mathbf{h})$ . In contrast, at superstructure reflection positions with uneven number equal signs of  $F_{\text{Sc}}(\mathbf{h})$  and  $F_{\text{Co}}(\mathbf{h})$  meet to yield a large absolute value of  $F(\mathbf{h})$ . Taking the absolute square of the summed structure factor profile leads to the observed characteristic intensity modulation for diffuse rods and pinpoint superstructure reflections along  $[h, 1.5, 0]$  in  $\text{Sc}_3\text{CoC}_4$  (see Fig. 7b).

\* georg.eickerling@physik.uni-augsburg.de

<sup>1</sup> A. P. Schlaus, M. S. Spencer, K. Miyata, F. Liu,

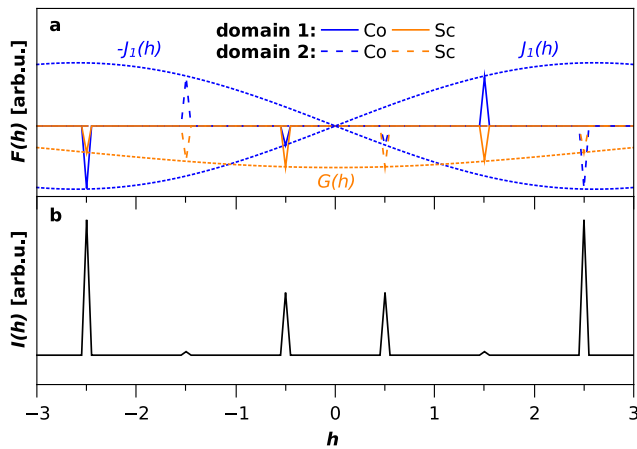


FIG. 7. Simulation<sup>78</sup> of the contributions to  $F(\mathbf{h})$  along  $[h, 1.5, 0]$  (referring to the orthorhombic HT-phase unit cell of  $\text{Sc}_3\text{CoC}_4$ ) for a simplified modulated  $\text{Sc}_3\text{CoC}_4$  structure (a): cobalt atom contributions are given in blue with tentative enveloping first-order Bessel functions  $J_1(h)$  and  $-J_1(h)$ . Scandium atom contributions are given in red with an enveloping Gaussian function  $G(h)$  as approximation for the angle-dependence of the atomic scattering factor of scandium. Scattering due to domain 1 is signified by solid lines, scattering due to domain 2 by hatched lines. The summed up and squared structure factor contributions (b) reproduce the experimentally observed intensity alternation scheme along  $[h, 1.5, 0]$ .

- X. Wang, I. Datta, M. Lipson, A. Pan, and X.-Y. Zhu, *Nat. Commun.* **10**, 265 (2019).
- <sup>2</sup> D. Ji, S. Cai, T. R. Paudel, H. Sun, C. Zhang, L. Han, Y. Wei, Y. Zang, M. Gu, Y. Zhang, W. Gao, H. Huyan, W. Guo, D. Wu, Z. Gu, E. Y. Tsymbal, P. Wang, Y. Nie, and X. Pan, *Nature* **570**, 87 (2019).
- <sup>3</sup> A. Meerschaut and J. Rouxel, *J. Less-Common Met.* **39**, 197 (1975).
- <sup>4</sup> J. L. Hodeau, M. Marezio, C. Roucau, R. Ayroles, A. Meerschaut, J. Rouxel, and P. Monceau, *J. Phys. C: Solid State Phys.* **11**, 4117 (1978).
- <sup>5</sup> M. N. Regueiro, J.-M. Mignot, and D. Castello, *EPL* **18**, 53 (1992).
- <sup>6</sup> L. Yang, Y. Tao, J. Liu, C. Liu, Q. Zhang, M. Akter, Y. Zhao, T. T. Xu, Y. Xu, Z. Mao, Y. Chen, and D. Li, *Nano Lett.* **19**, 415 (2019).
- <sup>7</sup> J. Graham and A. D. Wadsley, *Acta Cryst.* **20**, 93 (1966).
- <sup>8</sup> G. Travaglini, P. Wachter, J. Marcus, and C. Schlenker, *Solid State Commun.* **37**, 599 (1981).
- <sup>9</sup> J. P. Pouget, S. Kagoshima, C. Schlenker, and J. Marcus, *J. Physique Lett.* **44**, 113 (1983).
- <sup>10</sup> K. Inagaki and S. Tanda, *Phys. Rev. B* **97**, 115432 (2018).
- <sup>11</sup> K. S. Novoselov, A. K. Geim, S. V. Morozov, D. Jiang, Y. Zhang, S. V. Dubonos, I. V. Grigorieva, and A. A. Firsov, *Science* **306**, 666 (2004).
- <sup>12</sup> Y. Cao, V. Fatemi, S. Fang, K. Watanabe, T. Taniguchi, E. Kaxiras, and P. Jarillo-Herrero, *Nature* **556**, 43 (2018).
- <sup>13</sup> P. M. Williams, G. S. Parry, and C. B. Scrub, *Phil. Mag.* **29**, 695 (1974).
- <sup>14</sup> S.-H. Lee, J. S. Goh, and D. Cho, *Phys. Rev. Lett.* **122**, 106404 (2019).
- <sup>15</sup> H. P. Hughes, *J. Phys. C: Solid State Phys.* **10**, L319 (1977).
- <sup>16</sup> G.-J. Shu, Y. Zhou, M.-Y. Kao, C. J. Klingshirn, M. R. S. Huang, Y.-L. Huang, Y. Liang, W. C. H. Kuo, and S.-C. Liou, *Appl. Phys. Lett.* **114**, 202103 (2019).
- <sup>17</sup> S. Pyon, K. Kudo, and M. Nohara, *J. Phys. Soc. Jpn.* **81**, 053701 (2012).
- <sup>18</sup> H. Oike, M. Kamitani, Y. Tokura, and F. Kagawa, *Sci. Adv.* **4**, eaau3489 (2018).
- <sup>19</sup> M. Ido, Y. Okayama, T. Ijiri, and Y. Okajima, *J. Phys. Soc. Jpn.* **59**, 1341 (1990).
- <sup>20</sup> S. Yasuzuka, K. Murata, T. Fujimoto, M. Shimotori, and K. Yamaya, *J. Phys. Soc. Jpn.* **74**, 1782 (2005).
- <sup>21</sup> P. Monceau, *Adv. Phys.* **61**, 325 (2012).
- <sup>22</sup> A. Kiswandhi, J. S. Brooks, H. B. Cao, J. Q. Yan, D. Mandrus, Z. Jiang, and H. D. Zhou, *Phys. Rev. B* **87**, 121107 (2013).
- <sup>23</sup> J. J. Yang, Y. J. Choi, Y. S. Oh, A. Hogan, Y. Horibe, K. Kim, B. I. Min, and S.-W. Cheong, *Phys. Rev. Lett.* **108**, 116402 (2012).
- <sup>24</sup> W. Jeitschko, M. H. Gerress, R.-D. Hoffmann, and S. Lee, *J. Less-Common Met.* **156**, 397 (1989).
- <sup>25</sup> A. Tsokol, O. I. Bodak, and E. P. Marusin, *Kristallografiya* **31**, 788 (1986).
- <sup>26</sup> B. Rohrmoser, G. Eickerling, M. Presnitz, W. Scherer, V. Eyert, R.-D. Hoffmann, U. C. Rodewald, C. Vogt, and R. Pöttgen, *J. Am. Chem. Soc.* **129**, 9356 (2007).
- <sup>27</sup> W. Scherer, C. Hauf, M. Presnitz, E.-W. Scheidt, G. Eickerling, V. Eyert, R.-D. Hoffmann, U. C. Rodewald, A. Hammerschmidt, C. Vogt, and R. Pöttgen, *Angew. Chem. Int. Ed.* **49**, 1578 (2010).
- <sup>28</sup> E.-W. Scheidt, C. Hauf, F. Reiner, G. Eickerling, and W. Scherer, *J. Phys.: Conf. Ser.* **273**, 012083 (2011).
- <sup>29</sup> W. Scherer, G. Eickerling, C. Hauf, M. Presnitz, E.-W. Scheidt, V. Eyert, and R. Pöttgen, *Modern Charge-Density Analysis*, 1st ed., edited by C. Gatti and P. Macchi (Springer Netherlands, 2012) Chap. 10, pp. 359–385.
- <sup>30</sup> G. Eickerling, C. Hauf, E.-W. Scheidt, L. Reichardt, C. Schneider, A. Muñoz, S. Lopez-Moreno, A. H. Romero, F. Porcher, G. André, R. Pöttgen, and W. Scherer, *Z. Anorg. Allg. Chem.* **639**, 1985 (2013).
- <sup>31</sup> M. He, C. H. Wong, D. Shi, P. L. Tse, E.-W. Scheidt, G. Eickerling, W. Scherer, P. Sheng, and R. Lortz, *J. Phys.: Condens. Matter* **27**, 075702 (2015).
- <sup>32</sup> E. Wang, X. Zhu, and H.-W. Wen, *EPL* **115**, 27007 (2016).
- <sup>33</sup> C. Vogt, R.-D. Hoffmann, U. C. Rodewald, G. Eickerling, M. Presnitz, V. Eyert, W. Scherer, and R. Pöttgen, *Inorg. Chem.* **48**, 6436 (2009).
- <sup>34</sup> C. Zhang, J. S. Tse, K. Tanaka, and H.-Q. Lin, *EPL* **100**, 67003 (2012).
- <sup>35</sup> C. D. Haas, *Strukturelle und physikalische Charakterisierungen niederdimensionaler Metallborocarbide und Metallcarbide*, Ph.D. thesis, University of Augsburg (2019).
- <sup>36</sup> See Supplemental Material at [URL will be inserted by publisher] for full experimental details and all data recorded between room temperature and 12 K.
- <sup>37</sup> J. Cosier and A. M. Glazer, *J. Appl. Cryst.* **19**, 105 (1986).
- <sup>38</sup> A. Reisinger, N. Trapp, I. Krossing, S. Altmannshofer, V. Herz, M. Presnitz, and W. Scherer, *Angew. Chem. Int. Ed.* **46**, 8295 (2007).
- <sup>39</sup> G. Kresse and J. Furthmüller, *Comput. Mater. Sci.* **6**, 15 (1996).
- <sup>40</sup> G. Kresse and J. Furthmüller,



- Phys. Rev. B **54**, 11169 (1996).
- <sup>41</sup> G. Kresse and J. Hafner, Phys. Rev. B **49**, 14251 (1994).
- <sup>42</sup> G. Kresse and J. Hafner, Phys. Rev. B **47**, 558 (1993).
- <sup>43</sup> J. P. Perdew, K. Burke, and M. Ernzerhof, Phys. Rev. Lett. **77**, 3865 (1996).
- <sup>44</sup> J. P. Perdew, K. Burke, and M. Ernzerhof, Phys. Rev. Lett. **78**, 1396 (1997).
- <sup>45</sup> A. Togo and I. Tanaka, Scr. Mater. **108**, 1 (2015).
- <sup>46</sup> B. Wehinger and A. Mirone, *ab2tids*, ESRF The European Synchrotron (2013), <http://ftp.esrf.fr/scisoft/AB2TDS/>.
- <sup>47</sup> An account of the employed image analysis techniques for the extraction of  $I_{XRD}(T)$  from experimental X-ray diffraction data is given in the Supplemental Material at [URL will be inserted by publisher].
- <sup>48</sup> D. E. Moncton, J. D. Axe, and F. J. DiSalvo, Phys. Rev. Lett. **34**, 734 (1975).
- <sup>49</sup> D. E. Moncton, J. D. Axe, and F. J. DiSalvo, Phys. Rev. B **16**, 801 (1977).
- <sup>50</sup> P. M. Williams, *Crystallography and Crystal Chemistry of Materials with Layered Structures*, edited by H. Lagergren, Springer, Dordrecht, 1976, Chap. 2, pp. 51–92.
- <sup>51</sup> C. Snow, J. Karpus, S. L. Cooper, T. Kidd, and T.-C. Chiang, Phys. Rev. Lett. **91**, 136402 (2003).
- <sup>52</sup> A. F. Kusmartseva, B. Sipoš, H. Berger, L. Forro, and E. Tutiš, Phys. Rev. Lett. **103**, 236401 (2009).
- <sup>53</sup> S. Sugai, K. Murase, S. Uchida, and S. Tanaka, Solid State Commun. **35**, 433 (1980).
- <sup>54</sup> N. Wakabayashi, H. Smith, K. Woo, and F. Brown, Solid State Commun. **28**, 923 (1978).
- <sup>55</sup> M. Holt, P. Zschack, H. Hong, M. Chou, and T.-C. Chiang, Phys. Rev. Lett. **86**, 3799 (2001).
- <sup>56</sup> F. J. Di Salvo, D. E. Moncton, and J. V. Waszczak, Phys. Rev. B **14**, 4321 (1976).
- <sup>57</sup> F. C. Brown, Physica B+C **99**, 264 (1980).
- <sup>58</sup> T. E. Kidd, T. Miller, M. Y. Chou, and T.-C. Chiang, Phys. Rev. Lett. **88**, 226402 (2002).
- <sup>59</sup> Y. I. Joe, X. Chen, P. Ghaemi, K. Finkelstein, G. de La Peña, Y. Gan, J. Lee, S. Yuan, J. Geck, G. MacDougall, T. Chiang, S. Cooper, E. Fradkin, and P. Abbamonte, Nat. Phys. **10**, 421 (2014).
- <sup>60</sup> C. B. Scruby, P. M. Williams, and G. S. Parry, Phil. Mag. **31**, 255 (1975).
- <sup>61</sup> J. P. Pouget, C. R. Phys. **17**, 332 (2016).
- <sup>62</sup> J. P. Pouget, R. Moret, A. Meerschaut, L. Guemas, and J. Rouxel, J. Phys. Colloques **44**, C3 (1983).
- <sup>63</sup> K. Ishida and G. Honjo, J. Phys. Soc. Jpn. **34**, 1279 (1973).
- <sup>64</sup> R. Xu and T. C. Chiang, Z. Kristallogr. Cryst. Mater. **220**, 1009 (2005).
- <sup>65</sup> The fact that the frequencies along the branch remain positive and the calculations do not predict the instability of the HT-phase most likely highlights the shortcomings of the standard GGA functional employed within this study to properly resolve the very flat energy surface region separating the HT- and LT-phase of  $\text{Sc}_3\text{CoC}_4$ .
- <sup>66</sup> C. Milesi-Brault, C. Toulouse, E. Constable, H. Aramberri, V. Simonet, S. de Brion, H. Berger, L. PaoLasini, A. Bosak, J. Íñiguez, and M. Guennou, Phys. Rev. Lett. **124**, 097603 (2020).
- <sup>67</sup> Key properties of the phonon dispersion remain unaffected by this problem as is demonstrated in the Supplemental Material at [URL will be inserted by publisher].
- <sup>68</sup> A plot of the phonon dispersion for the LT-phase structure of  $\text{Sc}_3\text{CoC}_4$  can be found in the Supplemental Material at [URL will be inserted by publisher].
- <sup>69</sup> E. Constable, S. Raymond, S. Petit, E. Ressouche, F. Bourdarot, J. Debray, M. Josse, O. Faugère, H. Berger, S. de Brion, and V. Simonet, Phys. Rev. B **96**, 014413 (2017).
- <sup>70</sup> R. B. Neder and T. Proffen, *Diffuse Scattering and Defect Structure Simulations*, 1st ed. (Oxford University Press, 2008) Chap. 6.2, pp. 75–79.
- <sup>71</sup> C. Giacovazzo, *Fundamentals of Crystallography*, 3rd ed., edited by C. Giacovazzo (Oxford University Press, 2011) Chap. 4.5, pp. 251–254.
- <sup>72</sup> Only the relative phase of the cobalt and scandium atom displacements is of interest for the final value of  $F(\mathbf{h})$ . Thus, the value of  $\phi$  for either the cobalt or the scandium atom displacements may be chosen arbitrarily as 0 or  $\pi$ .
- <sup>73</sup> A wave vector  $\mathbf{q} = (0.5, 0.5, p)^T$  must be used in the calculation of the superstructure reflection intensity along arbitrary lines  $[h, 1.5, p]$  parallel to  $[h, 1.5, 0]$ .
- <sup>74</sup> In the present simplified structure containing only cobalt atoms, two cobalt atoms at the fractional coordinates  $(0, 0.5, 0)$  and  $(0.5, 0, 0.5)$  have to be taken into account in the calculation of  $G_{\text{Co}}(\mathbf{h} \pm \mathbf{q})$ .
- <sup>75</sup> This is the situation found in the LT structure of  $\text{Sc}_3\text{CoC}_4$  published earlier, see Ref. 30.
- <sup>76</sup> Only the strongly displaced scandium atoms at the fractional coordinates  $(0.5, 0, 0)$  and  $(0, 0.5, 0.5)$  are taken into account.
- <sup>77</sup> More precisely, a twofold rotation of the diffraction pattern about  $a^*$  has to be performed corresponding to a twofold rotation about  $a$  as twin law in real-space.
- <sup>78</sup> T. Proffen and R. B. Neder, J. Appl. Cryst. **30**, 171 (1997).

# Supporting Information for: Evidence for a soft-phonon mode driven Peierls-type distortion in $\text{Sc}_3\text{CoC}_4$

Jan Langmann,<sup>1</sup> Christof Haas,<sup>1</sup> Emmanuel Wenger,<sup>2</sup>

Dominik Schaniel,<sup>2</sup> Wolfgang Scherer,<sup>1</sup> and Georg Eickerling<sup>1,\*</sup>

<sup>1</sup>*University of Augsburg, Institut für Physik, Universität Augsburg,  
Universitätsstraße 1, D-86159 Augsburg, Germany*

<sup>2</sup>*Universit de Lorraine, CNRS, CRM2, F-54000 Nancy, France*

(Dated: September 9, 2020)

## CONTENTS

I. Investigated samples	3
II. X-ray diffraction experiments	8
III. Twinning	9
IV. Generation of reciprocal-space maps	12
V. Temperature-dependent reciprocal-space maps	13
VI. Temperature-dependent intensity profiles	15
VII. Extraction of scattering intensities	17
VIII. Simulations of thermal diffuse scattering (TDS)	18
References	21

## I. INVESTIGATED SAMPLES

Two types of  $\text{Sc}_3\text{CoC}_4$  single-crystals were investigated in this work: Needle-shaped single-crystals obtained according to methods described in Refs. 1–3 and platelet-like single-crystals from heat treatment of  $\text{Sc}_3\text{CoC}_4$  powder in a lithium flux.<sup>4</sup>

The needle-shaped single-crystals were used in the determination of the temperature-dependent X-ray scattering intensity of pinpoint superstructure reflections and the temperature-dependent electrical resistivity. Sample sizes were characterized by an approximate thickness of 20  $\mu\text{m}$  and an approximate length of 200  $\mu\text{m}$  (see Fig. S1a for a photographic image of a typical sample). Reconstructions of common reciprocal-space planes from room-temperature X-ray diffraction data (Figs. S1b-d) indicate high crystalline quality with only minor imperfections. Comparison with corresponding reciprocal-space planes at 150 K (Figs. S3a-c) underlines that the sample quality is not degraded by systematic twinning in the transition from the high-temperature to the low-temperature phase of  $\text{Sc}_3\text{CoC}_4$ .

Due to their larger size with an approximate thickness of 150  $\mu\text{m}$  and an approximate lateral extension of 300  $\mu\text{m}$  (see Fig. S2a for a photographic image of the sample) the platelet-like single-crystals were employed in the temperature-dependent tracking of diffuse X-ray scattering features. Significant, but non-interfering crystal imperfections are apparent from scattered intensity at non-indexed positions in reconstructed reciprocal-space planes at room-temperature (Figs. S2b-d) and 150 K (Figs. S3d-f).

In order to verify, that the type of the sample does not affect the results discussed in the main text, measurements were performed on both types of single-crystals. In analogy to the platelet-like single-crystals, weak diffuse rods can be recognized in the room-temperature reconstruction of the  $(h, 1.5, l)$ -plane for a needle-shaped single-crystal (Fig. S4). Complementarily, the characteristic two-step increase of the superstructure reflection intensity  $I_{XRD}(T)$  found for the needle-shaped single-crystals is reproduced by a platelet-like single-crystal (Fig. S5a). This also holds for the corresponding two jumps in the electrical resistivity  $\rho(T)$  (Fig. S5b). Sample size effects may account for the slight downward shift of the anomalies in  $I_{XRD}(T)$  and  $\rho(T)$  as compared to the needle-shaped single-crystals.<sup>5</sup> Notably, the abrupt nature of the lower anomaly in scattering intensity and electrical resistivity is further emphasized by a sizable temperature hysteresis between cooling and heating cycle for the platelet-like single-crystal.

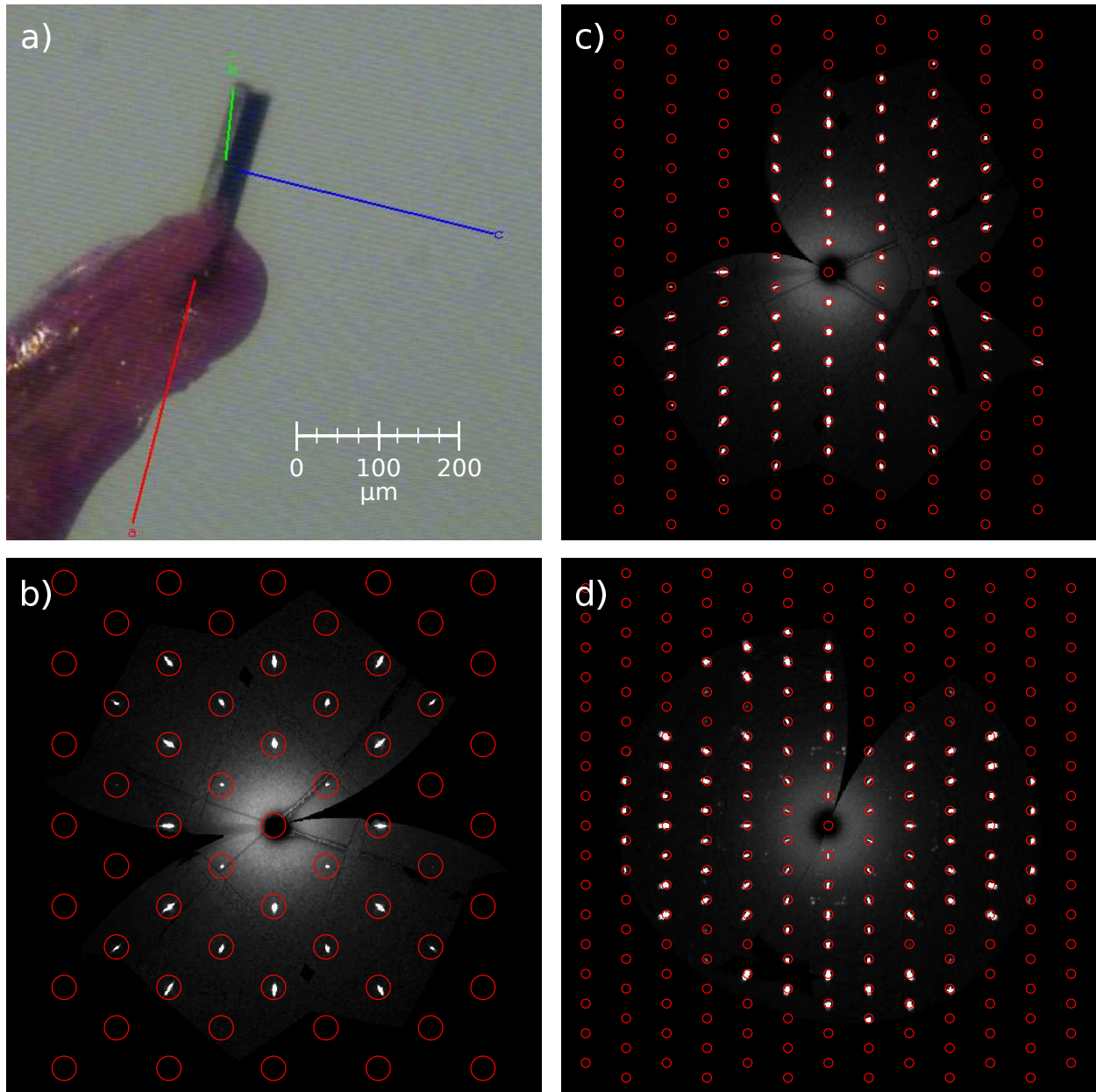


FIG. S1. (a) Photographic image of a typical needle-shaped  $\text{Sc}_3\text{CoC}_4$  single-crystal with crystal axes  $a$ ,  $b$  and  $c$  referring to the orthorhombic high-temperature phase unit cell indicated by coloured lines. Reconstructions of reciprocal-space planes (b)  $(hk0)$ , (c)  $(h0l)$  and (d)  $(0kl)$  from room-temperature X-ray diffraction data. Predicted reflection positions for HT- $\text{Sc}_3\text{CoC}_4$  are indicated by red circles.

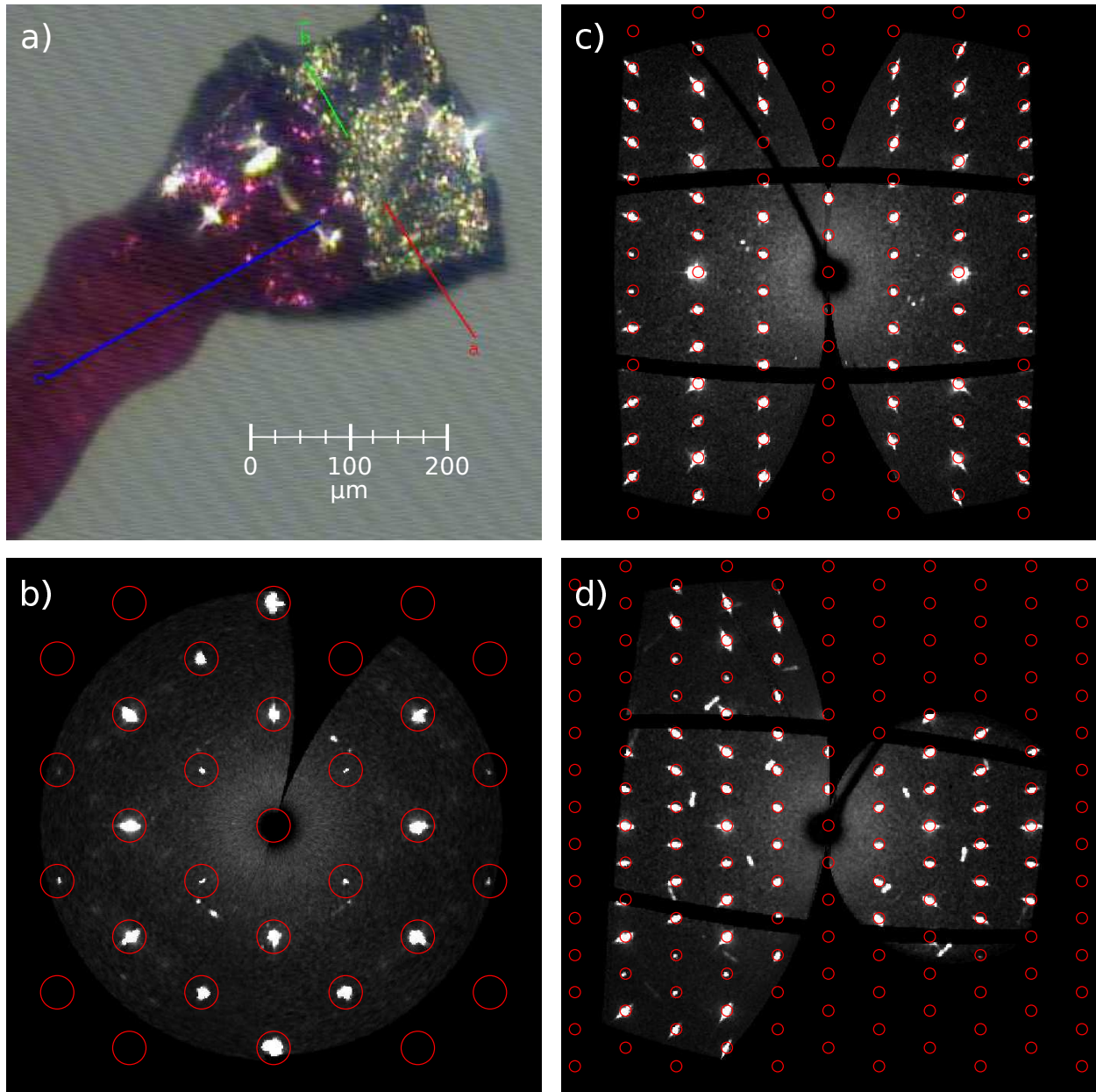


FIG. S2. (a) Photographic image of a platelet-like  $\text{Sc}_3\text{CoC}_4$  single-crystal with crystal axes  $a$ ,  $b$  and  $c$  referring to the orthorhombic high-temperature phase unit cell indicated by coloured lines. Reconstructions of reciprocal-space planes (b)  $(hk0)$ , (c)  $(h0l)$  and (d)  $(0kl)$  from room-temperature X-ray diffraction data. Predicted reflection positions are indicated by red circles.

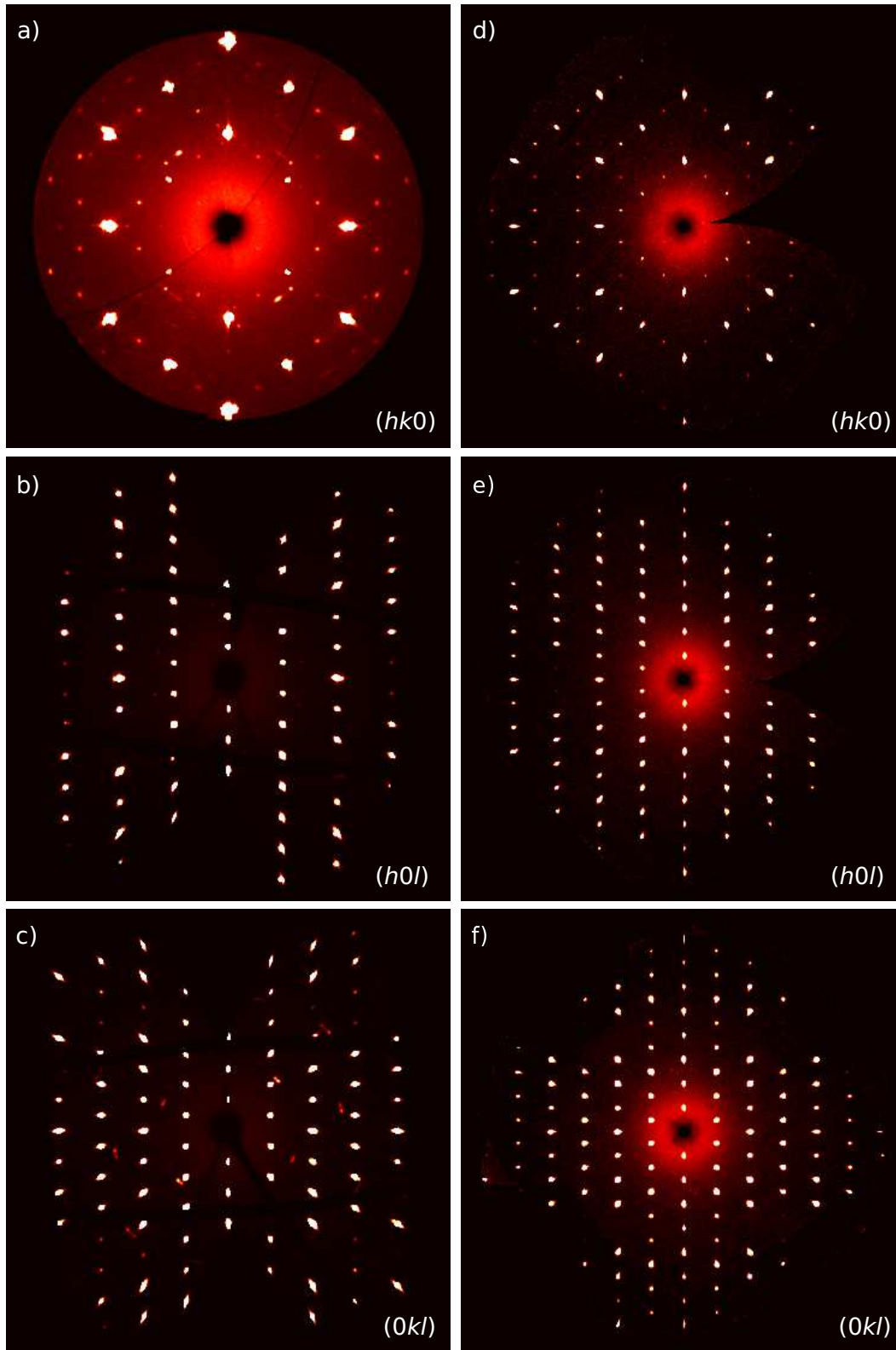


FIG. S3. Reconstructions of reciprocal-space planes  $(hk0)$ ,  $(h0l)$  and  $(0kl)$  from X-ray diffraction data for a platelet-like (a-c) and a needle-shaped  $\text{Sc}_3\text{CoC}_4$  single-crystal (d-f) at 150 K.

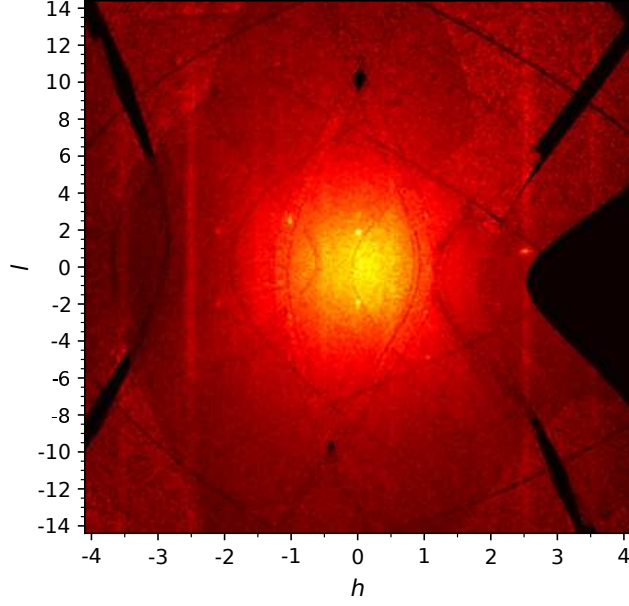


FIG. S4. Diffuse X-ray scattering features in the  $(h, 1.5, l)$ -plane for a needle-shaped single-crystal at room-temperature.

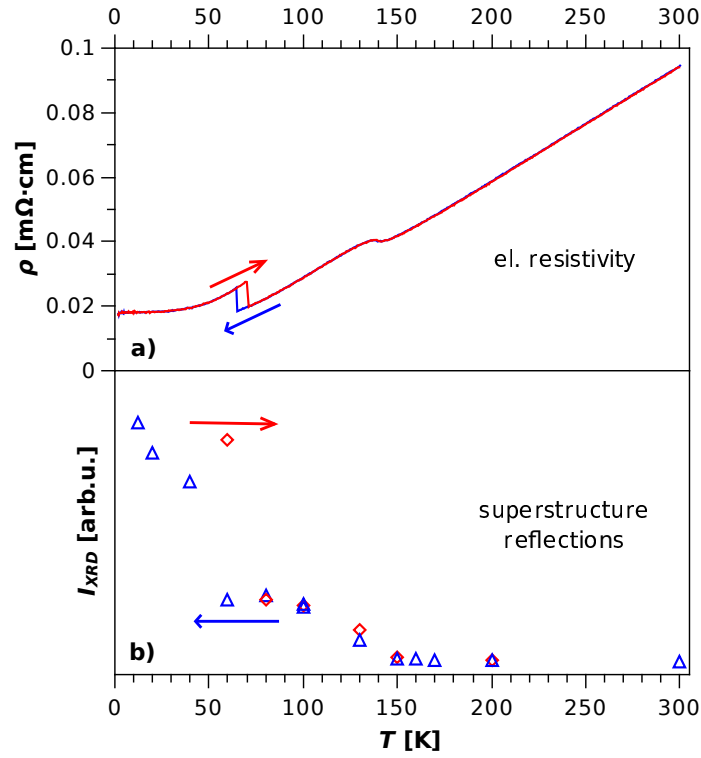


FIG. S5. Temperature-dependence of (a) the electrical resistivity  $\rho(T)$  and (b) the X-ray scattering intensity at superstructure reflection positions  $I_{XRD}(T)$  for a platelet-like single-crystal.



## II. X-RAY DIFFRACTION EXPERIMENTS

The temperature-dependence of the superstructure reflection intensity was determined by means of variable-temperature X-ray diffraction experiments on a single-crystalline needle of  $\text{Sc}_3\text{CoC}_4$  mounted on a capton mesh (MiTeGen). Depending on the temperature range two different experimental setups were employed: Sample temperatures in the range  $100 \text{ K} < T < 300 \text{ K}$  were reached on a CAD4  $\kappa$ -goniometer (BRUKER) fitted with a micro-focus tube (INCOATEC,  $\lambda(\text{Mo } K_\alpha) = 0.71073 \text{ \AA}$ ) and an open-flow  $\text{N}_2$  gas stream cooler (OXFORD).<sup>6</sup> The scattering intensity was recorded in  $\omega$ -scans ( $\Delta\omega = 2^\circ$ ,  $t = 582.5 \text{ s}$ ) on an XPAD 3.2 hybrid pixel detector.<sup>7</sup>  $\phi$ -scans ( $\Delta\phi = 0.5^\circ$ ,  $t = 30 \text{ min}$ ) in the temperature range  $10 \text{ K} < T < 100 \text{ K}$  were performed employing a Huber Eulerian cradle goniometer equipped with a modified closed-cycle He cryostat (ARS Cryo),<sup>8</sup> a MAR345 image plate detector (MARXPPTS), and a graphite monochromated FR591 rotating anode with molybdenum target (BRUKER,  $\lambda(\text{Mo } K_\alpha) = 0.71073 \text{ \AA}$ ).

An updated version of the latter setup featuring a micro-focus tube (INCOATEC,  $\lambda(\text{Ag } K_\alpha) = 0.56087 \text{ \AA}$ ) and a Pilatus3 R CdTe detector (DECTRIS) was used to collect long-exposure diffraction data for a lithium flux grown plate shaped single crystal of  $\text{Sc}_3\text{CoC}_4$  ( $12 \text{ K} < T < 100 \text{ K}$ ,  $\phi$ -Scans,  $\Delta\phi = 0.5^\circ$ ,  $t = 120 \text{ s}$ ). The sample was glued to a capton microloop (MiTeGen) using nail varnish. In the temperature range  $100 \text{ K} < T < 300 \text{ K}$  the closed-cycle He cryostat was replaced by an open-flow  $\text{N}_2$  gas stream cooler (OXFORD).<sup>6</sup>

### III. TWINNING

A direct observation of the twin domains in  $\text{Sc}_3\text{CoC}_4$ , e.g. by means of transmission electron microscopy (TEM), has not been achieved so far. Yet, inferences about the most probable orientation of the twin domain boundaries can be made on group theoretical grounds. Hints to the domain sizes come from single-crystal X-ray diffraction data.

As already pointed out by Vogt *et al.*<sup>2</sup>, systematic twinning in  $\text{Sc}_3\text{CoC}_4$  is induced by a  $t2$  step in the symmetry reduction pathway from the high-temperature to the low-temperature phase space-group  $I\frac{2}{m}\frac{2}{m}\frac{2}{m} \xrightarrow{t2} I11\frac{2}{m} \xrightarrow{i2} B11\frac{2}{m} (\hat{=} C1\frac{2}{m}1)$ . Thereby, twin domains with two distinct orientation states are formed. Consideration of the point groups of the involved space groups is sufficient for a determination of the twin operations relating the two possible twin domain orientations to each other.<sup>9</sup> Coset decomposition of the point group  $\frac{2}{m}\frac{2}{m}\frac{2}{m}$  ( $I\frac{2}{m}\frac{2}{m}\frac{2}{m}$ ) with respect to the point group  $11\frac{2}{m}$  ( $I11\frac{2}{m}$ ) yields the set of formally equivalent twin operations  $\{m_{[100]}, 2_{[100]}, m_{[010]}, 2_{[010]}\}$ . The mirror plane  $m_{[100]}$  has the highest chance of actually defining the macroscopic twin element that partitions the crystal into twin domains. This comes for two reasons: In the formation of twin domains mirror planes mostly take precedence over rotation axes.<sup>9</sup> Additionally, hypothetical twin domain boundaries aligning with the mirror plane  $m_{[010]}$  would bisect strongly covalent bonds in the infinite  $[\text{Co}(\text{C}_2)_2\text{Co}]$  ribbons of  $\text{Sc}_3\text{CoC}_4$ . Thus, a polysynthetic twin state with a stacking of twin domains along the  $a$ -axis of the high-temperature phase unit cell may be proposed.

An approximate upper boundary for the twin domain sizes can be obtained by twin integration of low-temperature single-crystal X-ray diffraction data with *EVAL14*<sup>10</sup> and subsequent data reduction with *TWINABS*.<sup>11</sup> Frame-wise scaling of collected reflection intensities as implemented in *TWINABS*<sup>11</sup> compensates for variations in absorption and irradiated crystal volume during sample rotation. The according scale-factors for each frame minimize intensity differences between symmetry-equivalent reflections and can be refined separately for each twin domain.<sup>12,13</sup> Taking into account the presumed polysynthetic twin domain arrangement the domain centers in  $\text{Sc}_3\text{CoC}_4$  cannot be moved to the rotation axis of the goniometer simultaneously. As a result, large twin domains with dimensions comparable to the X-ray beam diameter of approx.  $90 \mu\text{m}$  (FWHM)<sup>14</sup> should be affected by significant and domain-specific staggering around the rotation axis. This translates into a different variation of symmetry-equivalent reflection intensities for the individual twin domains and

a different behavior of the frame-wise scale-factor refined by *TWINABS*.<sup>11</sup>

If the rotation axis is oriented perpendicular to the plane of the domain walls, however, no differences in the domain-specific scale-factors can be observed and a domain size assessment is not possible. This is the case for the needle-shaped crystals whose long axis corresponding to the crystallographic *a*-axis was oriented approximately along the rotation axis (see crystal coordinate system in Fig. S1a). In contrast, the *c*-axis of a platelet-like crystal (dimensions  $140 \mu\text{m} \times 338 \mu\text{m} \times 350 \mu\text{m}$ ) was oriented parallel to the rotation axis, so that differences in the scale-factor variation may be expected in case of large twin domains. Yet, the obtained scale-factors for the twin domains at a temperature of 12 K vary almost perfectly in sync (see Fig. S6a). Such a behavior points to twin domains with a thickness much smaller than the beam diameter of  $90 \mu\text{m}$ .

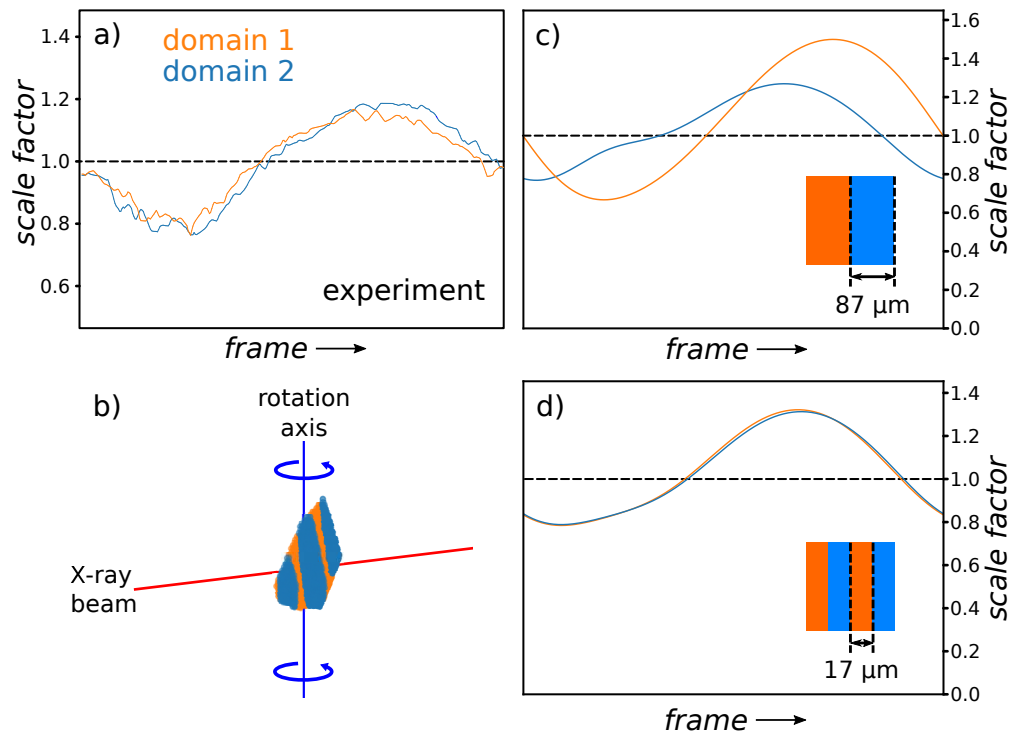


FIG. S6. (a) Frame-wise scale factor variation as obtained for a platelet-like crystal at 12 K and (b) simulation setup taking into account the crystal shape and a Gaussian beam-profile. Simulated scale factor variations for a domain thickness of  $87 \mu\text{m}$  and  $17 \mu\text{m}$  are given in c and d.

For a more accurate estimate of the maximum domain size the rotation of a twinned crystal in an X-ray beam with Gaussian profile ( $90 \mu\text{m}$  FWHM) was simulated. Thereby, the crystal shape was taken from the experiment and partitioned into lamellar domains of

varying thickness (see Fig. S6b). The intensity-weighted irradiated volumes of domains 1 and 2 were then sampled for different rotation angles. Conversion into scale-factors was achieved by normalization of the irradiated volumes to their average and subsequent calculation of the reciprocal values. As can be recognized from Figs. S6c and d, only twin domains with a thickness below approx.  $20 \mu\text{m}$  along the  $a$ -axis lead to a synchronous scale-factor variation.

#### IV. GENERATION OF RECIPROCAL-SPACE MAPS

For the creation of reciprocal layer reconstructions from experimental X-ray diffraction data the program *htd2predict* was used.<sup>15</sup> Similar to the program *XCAVATE*<sup>16</sup> it is capable of extracting scattering intensities in arbitrary pre-defined slices of reciprocal space from diffraction images. Unlike precession imaging relying on a defined specimen-alignment with respect to the rotation axis, no pre-orientation of the sample is needed for this purpose. The only requirement is the use of an area detector for the acquisition of the diffraction data. Thereby, the following procedure is used: First, the orientation matrix describing the crystal orientation with respect to the laboratory axis system is determined with the program *DIRAX*<sup>17</sup> and refined with the program *EVAL14*.<sup>10</sup> Building on this information the positions on the diffraction images corresponding to the points in the desired reciprocal-space layer are predicted. The detected scattering intensities at these positions are sampled and assigned to their reciprocal-space coordinates.

## V. TEMPERATURE-DEPENDENT RECIPROCAL-SPACE MAPS

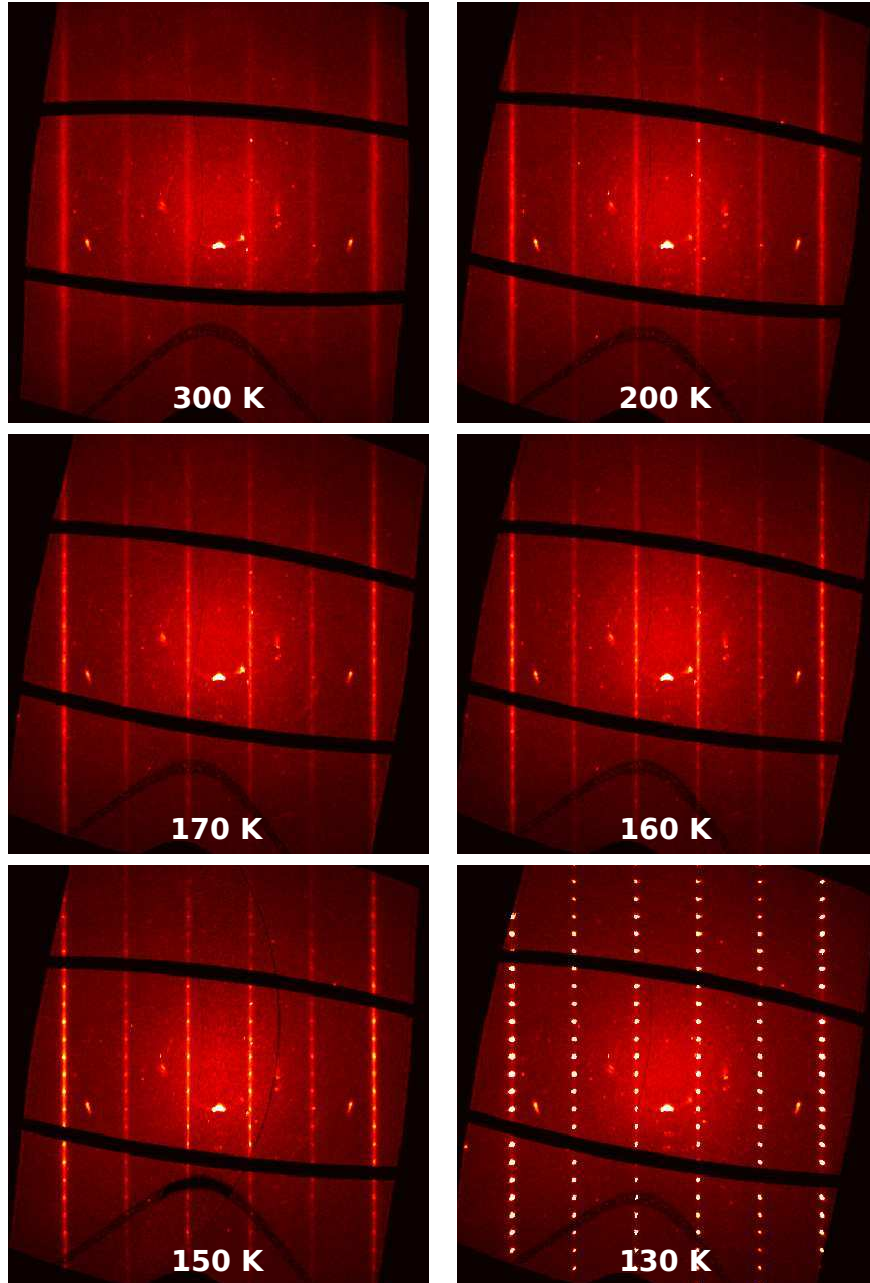


FIG. S7. Temperature-dependence of the X-ray scattering intensities in the  $(h, 1.5, l)$  reciprocal-space plane between 300 K and 130 K. Note that the Miller indices refer to the orthorhombic high-temperature phase unit cell. The X-ray scattering intensity at irregular positions can be attributed to imperfections in the investigated large single-crystal.

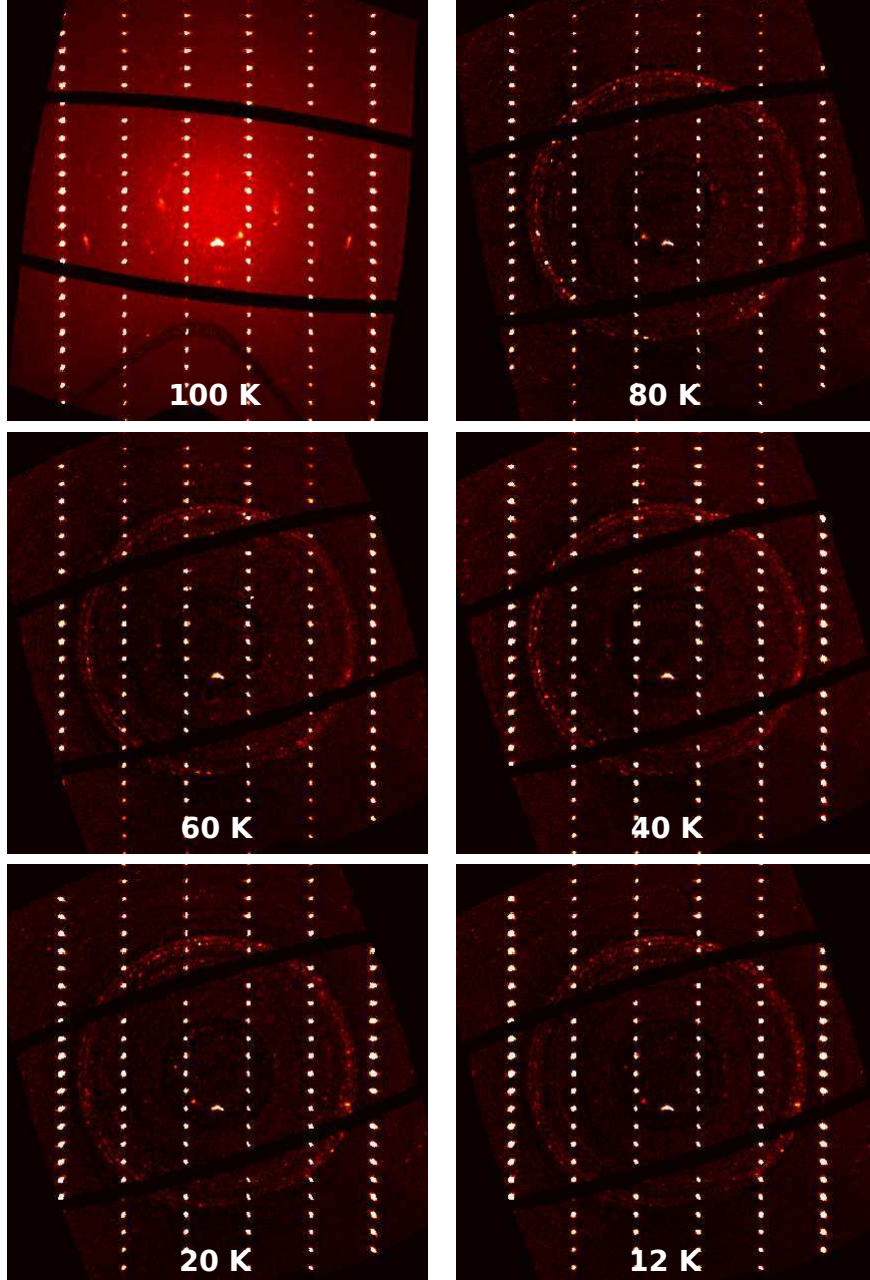


FIG. S8. Temperature-dependence of the X-ray scattering intensities in the  $(h, 1.5, l)$  reciprocal-space plane between 100 K and 12 K. Note that the Miller indices refer to the orthorhombic high-temperature phase unit cell. The X-ray scattering intensity at irregular positions can be attributed to imperfections in the investigated large single-crystal. Weak ring-shaped intensity between 80 K and 12 K is due to an incomplete subtraction of the scattering contributions from the beryllium vacuum shrouds of the closed-cycle He cryostat (see Sec. II).

## VI. TEMPERATURE-DEPENDENT INTENSITY PROFILES

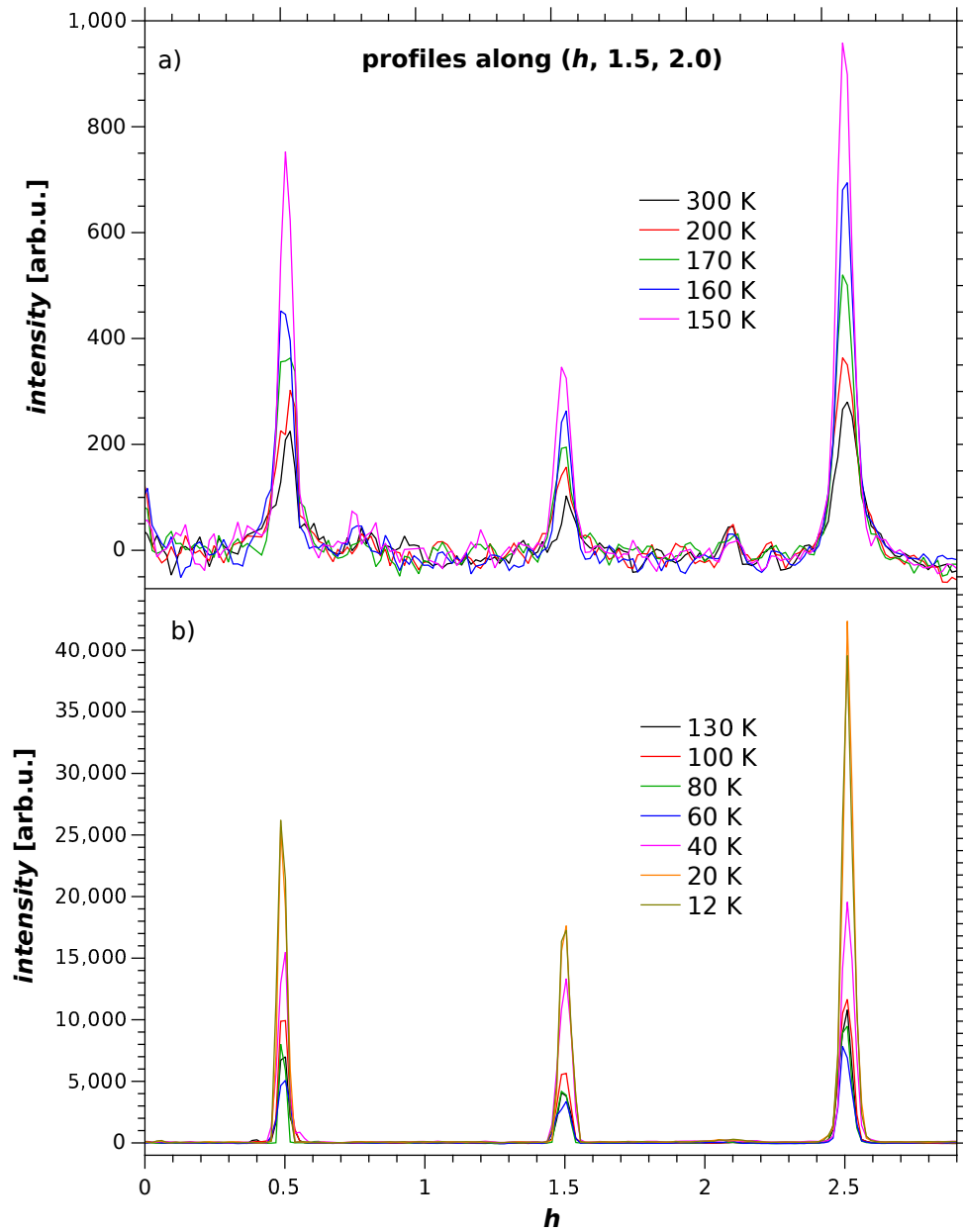


FIG. S9. Horizontal cuts through the reciprocal-space maps from Sec. V. The path  $(h, 1.5, 2.0)$  including superstructure reflection positions was sampled for temperatures between 300 K and 150 K (a) and between 130 K and 12 K (b). Note that the Miller indices refer to the orthorhombic high-temperature phase unit cell and that a Gaussian background was subtracted.



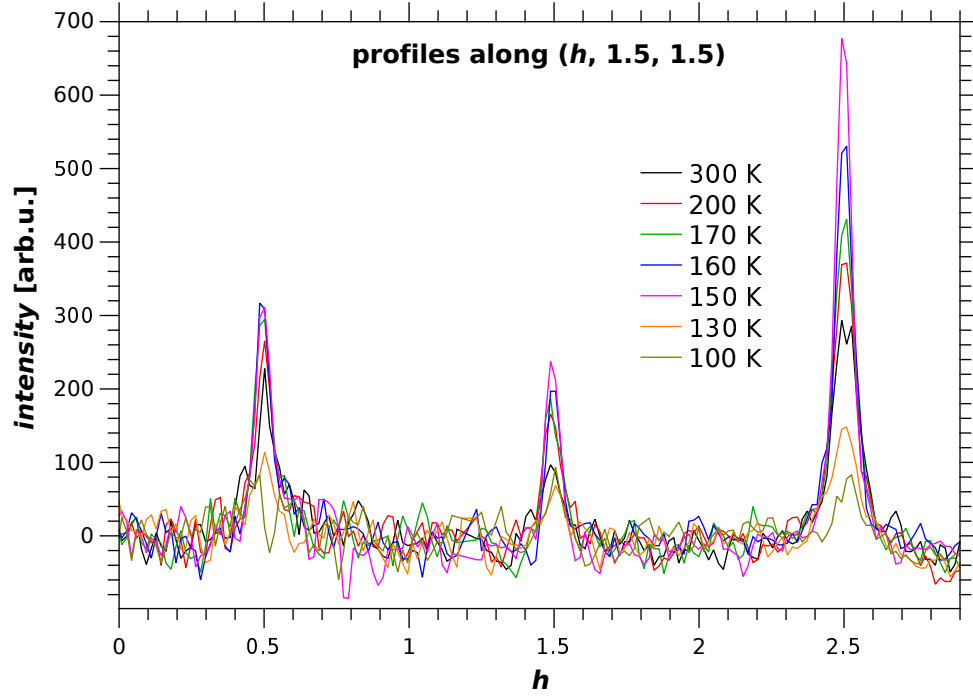


FIG. S10. Horizontal cuts through the reciprocal-space maps from Sec. V. The path  $(h, 1.5, 1.5)$  excluding superstructure reflection positions was sampled for temperatures between 300 K and 100 K. Note that the Miller indices refer to the orthorhombic high-temperature phase unit cell and that a Gaussian background was subtracted.

## VII. EXTRACTION OF SCATTERING INTENSITIES

Due to different characteristics of diffuse rods and superstructure reflections adapted approaches had to be used in the extraction of their intensities.

The superstructure reflections are pinpoint and spread only over few X-ray diffraction images collected in  $\phi$ -scanning mode. This situation allows the usage of single unprocessed diffraction images to track the temperature-dependent intensity of a representative  $(-1.5, 0.5, 0)$  reflection.<sup>18</sup> The intensity sampling was done using the program Imagej<sup>19</sup> by summing up the detected intensity of the pixels inside a quadratic box around the predicted position of the  $(-1.5, 0.5, 0)$  reflection. Therefrom, a background intensity obtained by multiplication of the average pixel intensity at the edges of the integration box with the number of contained pixels was subtracted. The usage of different  $\phi$ -increments of  $0.5^\circ$  and  $2.0^\circ$  per frame in the temperature ranges  $10 \text{ K} < T < 100 \text{ K}$  and  $100 \text{ K} < T < 300 \text{ K}$  was outbalanced by adding up four frames with  $0.5^\circ$  increment. Both temperature-dependent intensity data sets were scaled to the reflection intensity at 100 K.

The diffuse rods, by contrast, are weak and span a large number of X-ray diffraction images. Thus, the intensity extraction scheme was based on reciprocal-space reconstructions that were generated with the program *htd2predict*<sup>15</sup> (see Sec. IV). Thereby, the intensity at positions  $(2.5, 1.5, 0.5)$ ,  $(2.5, 1.5, 1.5)$  and  $(2.5, 1.5, 2.5)$ ,<sup>18</sup> *i.e.* midway between the superstructure reflection positions in a row along  $c^*$ , was sampled by a box integration method in analogy to the superstructure reflections. Due to their continuous nature along  $c^*$ , however, only the pixel intensity at the two edges of the integration box parallel to the diffuse rods was used in the determination of the subtracted background intensity. In a final step the intensities at all three positions were averaged.

## VIII. SIMULATIONS OF THERMAL DIFFUSE SCATTERING (TDS)

In this work the simulation of thermal diffuse scattering (TDS) contributions with the program *ab2tds*<sup>20</sup> relies on *ab-initio* dynamical matrices obtained by the finite-displacement method. Necessary Fourier interpolation of the dynamical matrix<sup>21</sup> during the simulation process may introduce artifacts such as the observed weak modulation of the diffuse rod intensity for the high-temperature (HT) phase of  $\text{Sc}_3\text{CoC}_4$  along the  $c^*$ -axis.

To ensure that the dynamical matrix is basically left intact by the Fourier interpolation step inelastic X-ray scattering (IXS) intensity maps for a temperature of 300 K were simulated in *ab2tds*.<sup>20</sup> By plotting the calculated variation of the inelastically scattered X-ray intensity  $I(E, \mathbf{Q})$  with energy transfer  $E$  and momentum transfer  $\mathbf{Q}$  salient features of the phonon dispersion should be reproduced. Differences may only arise due to the dependence of  $I(E, \mathbf{Q})$  on the scattering factors  $S_\alpha(\lambda, \mathbf{Q})$  for atoms  $\alpha$  and the scalar product  $\mathbf{Q} \cdot \mathbf{e}_{v\mathbf{Q}}^\alpha$  of momentum  $\mathbf{Q}$  and polarisation vector for phonon branch  $v$ . Additionally, folding of  $I(E, \mathbf{Q})$  with a resolution function leads to a blurring of details in the phonon dispersion.

Comparison of the simulated IXS intensity map for the HT-phase of  $\text{Sc}_3\text{CoC}_4$  in Fig. S11a with the unprocessed phonon dispersion in Fig. S11b shows excellent overall agreement. Most noteworthy, the soft phonon branch between the high-symmetry points W and T in the phonon dispersion reappears unaltered in the IXS intensity map. Vanishing of the IXS intensity for the phonon branches between  $\Gamma$  and R at approx. 120 meV may be caused by a small  $S_\alpha(\lambda, \mathbf{Q})$  or orthogonality of  $\mathbf{Q}$  and  $\mathbf{e}_{v\mathbf{Q}}^\alpha$  in this region. There is also good correspondence between the simulated IXS intensity map for the LT-phase of  $\text{Sc}_3\text{CoC}_4$  in Fig. S12a and the unprocessed phonon dispersion in Fig. S12b. Although high-energy regions of the IXS map suffer from weak intensity, the absence of a soft phonon branch in the LT-phase is clearly reflected.

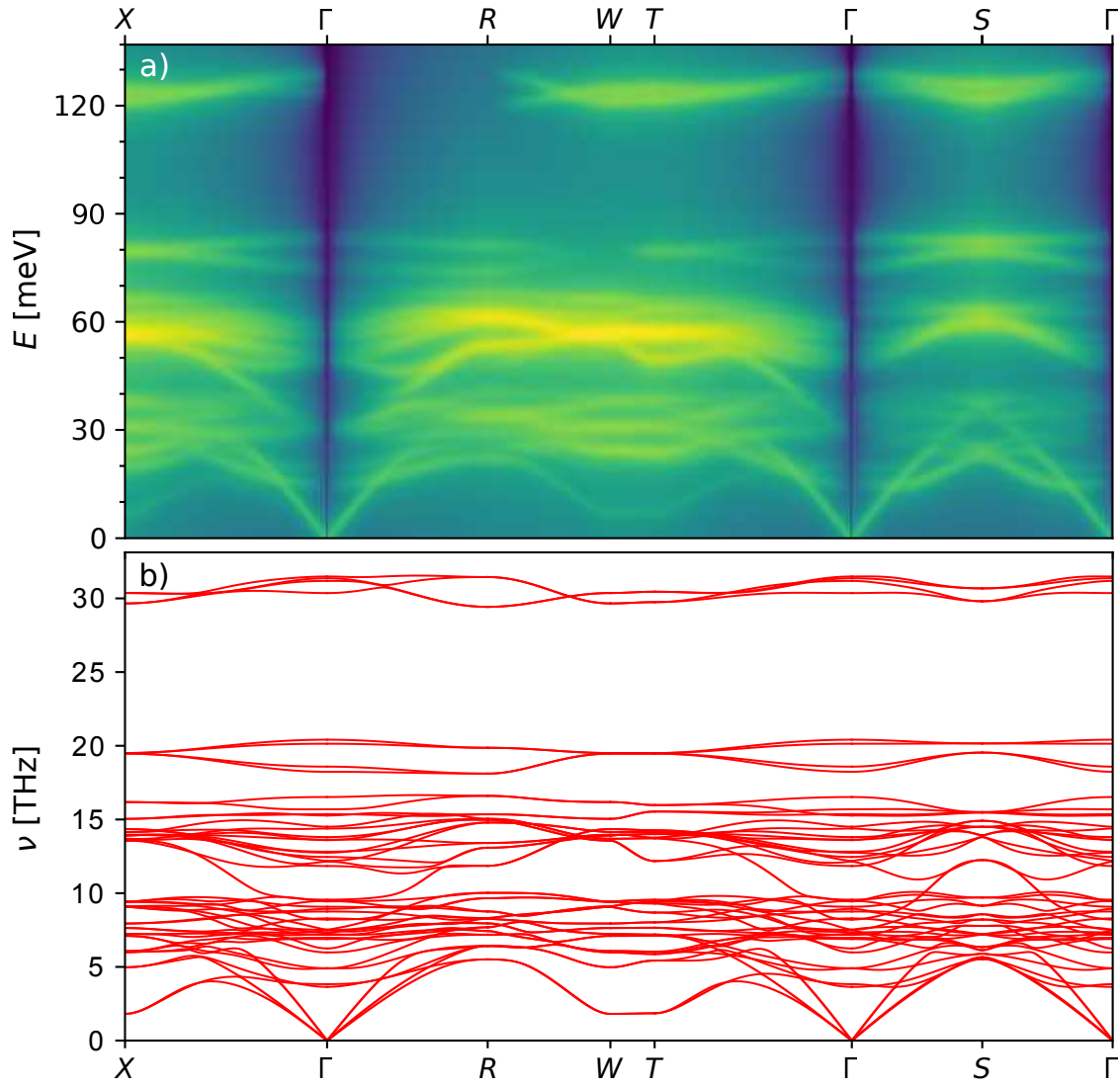


FIG. S11. (a) Simulated Inelastic X-ray scattering (IXS) map at 300 K and (b) unprocessed phonon dispersion relation for the high-temperature phase of  $\text{Sc}_3\text{CoC}_4$  along the same high-symmetry paths in the Brillouin zone.

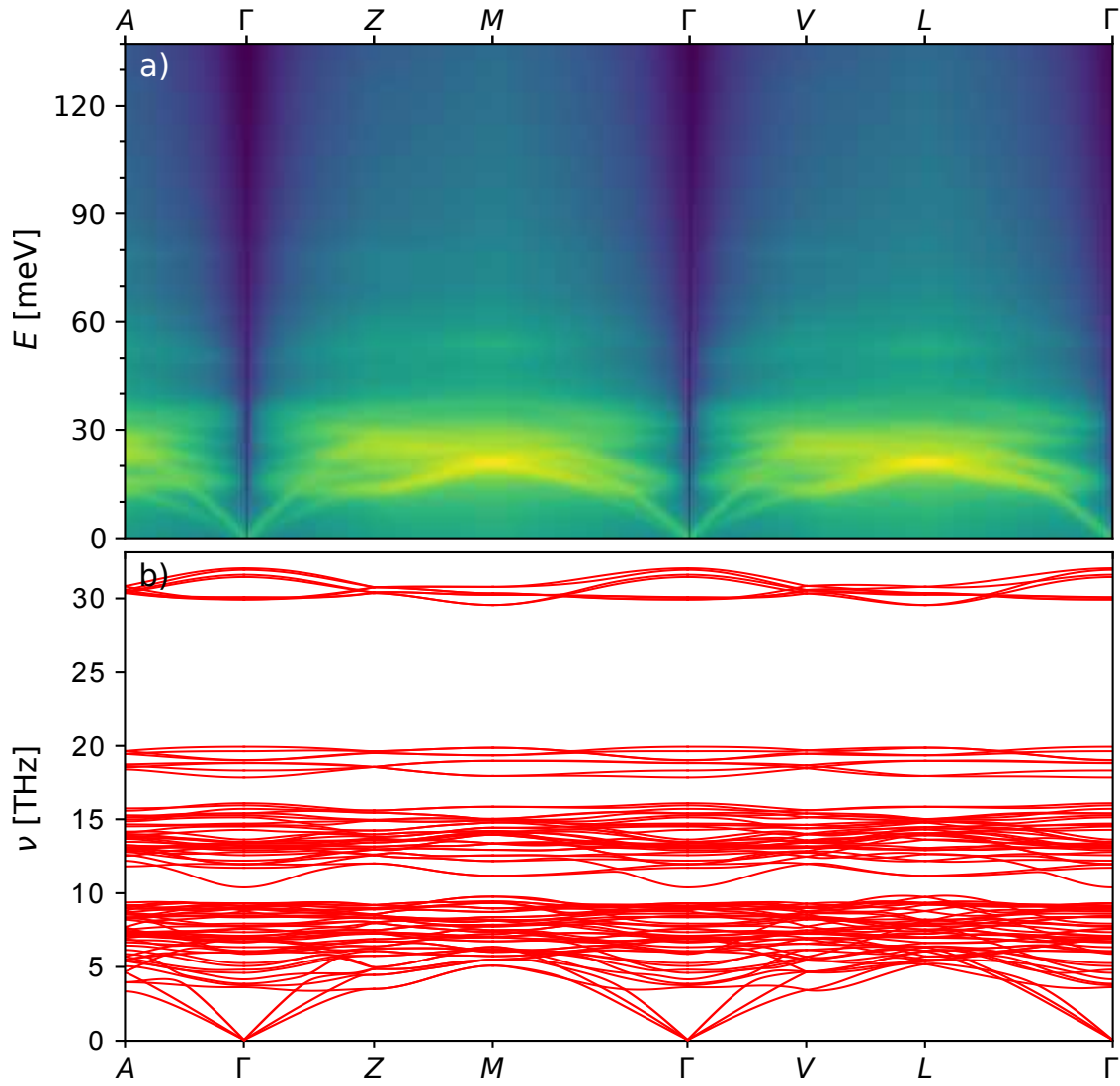


FIG. S12. (a) Simulated Inelastic X-ray scattering (IXS) map at 300 K and (b) unprocessed phonon dispersion relation for the low-temperature phase of  $\text{Sc}_3\text{CoC}_4$  along the same high-symmetry paths in the Brillouin zone.

- 
- \* georg.eickerling@physik.uni-augsburg.de
- <sup>1</sup> B. Rohrmoser, G. Eickerling, M. Presnitz, W. Scherer, V. Eyert, R.-D. Hoffmann, U. C. Rodewald, C. Vogt, and R. Pöttgen, *J. Am. Chem. Soc.* **129**, 9356 (2007).
- <sup>2</sup> C. Vogt, R.-D. Hoffmann, U. C. Rodewald, G. Eickerling, M. Presnitz, V. Eyert, W. Scherer, and R. Pöttgen, *Inorg. Chem.* **48**, 6436 (2009).
- <sup>3</sup> M. He, C. H. Wong, D. Shi, P. L. Tse, E.-W. Scheidt, G. Eickerling, W. Scherer, P. Sheng, and R. Lortz, *J. Phys.: Condens. Matter* **27**, 075702 (2015).
- <sup>4</sup> C. D. Haas, *Strukturelle und physikalische Charakterisierungen niederdimensionaler Metallborocarbide und Metallcarbide*, Ph.D. thesis, University of Augsburg (2019).
- <sup>5</sup> M. Natarajan, A. Das, and C. Rao, *Trans. Faraday Soc.* **65**, 3081 (1969).
- <sup>6</sup> J. Cosier and A. M. Glazer, *J. Appl. Cryst.* **19**, 105 (1986).
- <sup>7</sup> E. Wenger, S. Dahaoui, P. Alle, P. Parois, C. Palin, C. Lecomte, and D. Schaniel, *Acta Cryst.* **B70**, 783 (2014).
- <sup>8</sup> A. Reisinger, N. Trapp, I. Krossing, S. Altmannshofer, V. Herz, M. Presnitz, and W. Scherer, *Angew. Chem. Int. Ed.* **46**, 8295 (2007).
- <sup>9</sup> T. Hahn and H. Klapper, *International Tables for Crystallography*, 2nd ed., Vol. D (John Wiley & Sons, Ltd., 2014) Chap. 3.3, pp. 413–483.
- <sup>10</sup> A. J. M. Duisenberg, L. M. J. Kroon-Batenburg, and A. M. M. Schreurs, *J. Appl. Cryst.* **36**, 220 (2003).
- <sup>11</sup> L. Krause, R. Herbst-Irmer, G. M. Sheldrick, and D. Stalke, *J. Appl. Crystallogr.* **48**, 3 (2015).
- <sup>12</sup> G. M. Sheldrick, “Recent developments in twinabs,” (2007).
- <sup>13</sup> G. M. Sheldrick, “Data scaling with the bruker programs sadabs and twinabs,” (2015).
- <sup>14</sup> Incoatec GmbH, *I $\mu$ S for Ag-K $\alpha$  Radiation* (2015).
- <sup>15</sup> J. Langmann, A. Fischer, and G. Eickerling, *htd2predict*, University of Augsburg (2019).
- <sup>16</sup> M. A. Estermann and W. Steurer, *Phase Transit.* **67**, 165 (1998).
- <sup>17</sup> A. J. M. Duisenberg, *J. Appl. Cryst.* **25**, 92 (1992).
- <sup>18</sup> Referring to the unit cell of the high-temperature phase.
- <sup>19</sup> C. A. Schneider, W. S. Rasband, and K. W. Eliceiri, *Nat. Methods* **9**, 671 (2012).
- <sup>20</sup> B. Wehinger and A. Mirone, *ab2tds*, ESRF The European Synchrotron (2013),

<http://ftp.esrf.fr/scisoft/AB2TDS/>.

- <sup>21</sup> B. Wehinger, *On the combination of thermal diffuse scattering, inelastic x-ray scattering and ab initio lattice dynamics calculations*, Ph.D. thesis, Universite de Grenoble (2014).